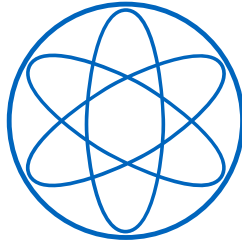


Physics Department



Information Field Theory for High Energy Astronomy

Diploma Thesis
by

Marco Selig

Technical University of Munich



Supervision: PD Dr. Ewald Müller
Dr. Torsten Enßlin

For my beloved family

Diana, Kristina & Peter
and
Gisela & Gerhard, Inge & Günter

Information Field Theory for High Energy Astronomy

Diploma Thesis
by

Marco Selig

Supervision: PD Dr. Ewald Müller
Dr. Torsten Enßlin

» Captain, the most elementary and valuable statement in science,
the beginning of wisdom, is, › I do not know ‹ . «

Lieutenant Commander Data, star date 42193.6

Abstract

The proper analysis of data is an inevitable necessity in all fields of physics. In high energy astronomy, where observations in the X- and γ -ray domain are performed, the data consist of information about the detected photons, i.e. their detection time, incidence angle, and frequency or energy. The numerous sources emitting X- and γ -ray photons can be classified into two phenomenological classes, diffuse and point sources.

Separating these source components from spatially resolved photon counts is a nontrivial task due to their superposition and the shot noise in the data. The main goal of this thesis is the reconstruction of the photon flux and its separation into diffuse and point-like components. In order to limit the complexity, the analysis is restricted to binned photon counts without energy information. In addition, an estimation of the uncertainties corresponding to the two signal components is required in order to judge the reliability of the results. Those uncertainties are encoded in an uncertainty covariance matrix, where in particular its diagonal describes the pixelwise uncertainty of the signal. However, the exact calculation of matrix diagonals is often computationally not feasible. Therefore, a way to improve stochastic estimates of matrix diagonals using inference methods is also addressed here.

The algorithm developed for the photon flux reconstruction and separation is derived using information field theory within the framework of a Bayesian probability theory. Here, the possible signal field configurations and their corresponding uncertainties are described naturally by means of probabilities. The minimum Gibbs free energy method is introduced and applied to the problem. This method combines the maximum a posteriori and the maximum entropy method in a thermodynamical inference scheme.

Mock simulations show a successful separation of diffuse and point-like components in the photon flux and a good agreement between the reconstructed and the original signals. Even faint point sources are reconstructed well. However, some prevailing numerical problems cause an inflated uncertainty estimation and inaccuracies in the small-scale reconstruction of the diffuse component. A number of possible improvements addressing these problems are suggested for future work.

Contents

1. Introduction	11
1.1. Overview	11
1.2. Structure of this thesis	14
2. Information field theory	16
2.1. Logic, Probabilities & Bayesics	16
2.2. Information & fields	19
2.3. Thermodynamical inference	21
2.3.1. Maximum a posteriori	22
2.3.2. Maximum entropy	23
2.3.3. Minimum Gibbs free energy	24
2.4. Generic filter	27
2.4.1. Generalized Wiener filter	27
2.4.2. Lack of spectral knowledge	30
3. Estimation of a matrix diagonal	32
3.1. Problem	33
3.1.1. Exact matrix diagonal	33
3.2. Probing estimate	34
3.3. Bayesian estimate	35
3.3.1. Forward model	35
3.3.2. Inference algorithm	36
3.4. Verification & application	38
3.4.1. Numerical experiments	38
3.4.2. Faraday sky uncertainty	40
3.5. Conclusions	41
4. Photon flux reconstruction & separation	43
4.1. Problem	44
4.1.1. Poisson distribution & shot noise	45
4.2. Data model setup	45
4.2.1. Poisson distributed data	45
4.2.2. Signal response	46
4.2.3. Diffuse signal & spectral parameters	47
4.2.4. Point-like signal	48
4.2.5. Data model summary	49
4.3. Gibbs free energy of the combined photon flux	50
4.3.1. Derivation	50
4.3.2. Self-consistent solution	54

CONTENTS

4.3.3. Gradient approach	56
4.4. Application results	58
4.4.1. Tempering	58
4.4.2. Comparison	62
4.5. Conclusions	63
5. Conclusions & outlook	64
A Notation	65
A1. Basic Notation	65
A2. Special Notation	66
A2.1. Componentwise operations	66
A2.2. Diagonal operator	66
B Spherical Harmonics	67
B1. Basics	67
B2. Statistical isotropy	67
B2.1. Power spectrum	68
B2.2. Parameterization	68
C Higher order corrections	69
Acknowledgments	71
References	74
Publication note	75

List of Tables

1	Boolean algebra	17
2	Step size selection criteria	58

List of Figures

1	Resulting maps from the trivial case	39
2	Result overview of the trivial case	39
3	Diagonals from the realistic case	40
4	Result overview of the realistic case	40
5	Resulting maps from the galactic Faraday depth reconstruction . . .	41
6	Result overview of the galactic Faraday depth reconstruction . . .	41
7	Data generation chain	50
8	Sketch of the Gibbs free energy landscape	57
9	Diffuse signal power spectra	59
10	Reconstruction results at $T = 0.05$	60
11	Reconstruction results at $T = 0.5$	61
12	Comparison of the flux from diffuse sources	62
13	Comparison of the flux from point sources	63

List of Acronyms

CPU	Central processing unit
IFT	Information field theory
MAP	Maximum a posteriori
ME	Maximum entropy
MMSE	Minimum mean square error
PDF	Probability density function
PSF	Point spread function

1. Introduction

1.1. Overview

Physics is based on the interplay of theory and experiment. Any theoretical prediction is in question as long as it is not confirmed or refuted by an appropriate experiment, and any experimental result is of minor significance as long as it is not explained by a novel or established theory. A theory is well-defined by all included assumptions and hypotheses from which propositions and predictions are deduced. If a consistent theory is in question due to experimental outcomes, then either the theoretical assumptions are inadequate or the experiment is not fully understood. The proper analysis of experimental data is thus mandatory.

All experiments are subject to uncertainties, if only e.g. on the level of the Heisenberg uncertainty principle. Therefore, any relevant uncertainty needs to be taken into account in order to obtain significant conclusions. This is of importance especially in the present era, where on the one hand high precision experiments are performed, and on the other hand measurements on smaller and smaller scales are targeted, e.g. the detection of gravitational waves [26] or of the neutron's electric dipole moment.

In the field of high energy astronomy, which covers observations in the X- and γ -ray domain, a series of surveys have been performed in the last six decades. The most recent instruments in this series are the orbital observatories Chandra, XMM-Newton, Integral, and Fermi. Technical innovations enable data acquisition with higher and higher spatial resolution. Nevertheless, the photons emitted from several astrophysical sources are superimposed in the data and ad hoc partitioning is not possible. Thus, the question of how to separate different emission components arises.

Many emission components can be coarsely categorized as being either diffuse or point-like structures which in turn exhibit very distinctive features. The latter are shaped like broadened peaks that nevertheless may differ in their brightness from outshining to faint or barely detectable. The list of sources that cause such characteristic point-like structures is long. The most prominent amongst them are the distant active galactic nuclei, some of which are so bright even in the optical bands that they appear quasi stellar, the so called quasars. Diffuse sources, on the other hand, spread out smoothly across wide areas of the angular sky. Black-body radiation, bremsstrahlung, synchrotron radiation, inverse Compton scattering, radioactive and pion decay after hadronic interactions, as well as electron-positron annihilation are the main processes leading to radiation in the X- and γ -ray domain. Nevertheless, diffuse emission is everything else than a nuisance, e.g. the recent discovery of the two giant γ -ray bubbles in the Milky Way revealed processes that took place in the galactic center of our own galaxy [30, 6].

Since the evolution times of astrophysical objects are usually much larger than a human's lifetime, we can usually only observe a particular object in a single state. Therefore, it is necessary to examine a population of objects in order to confirm or refute astrophysical theories describing their genesis or evolution. As a result, the identification of those objects is essential in astrophysics. The detection precision of point sources depends directly on the correct estimation of diffuse foreground or background fluxes. Thus, for each data bin, one can ask whether the detected signal stems from diffuse or point-like sources or a combination of both, and how certain the former answer is.

The formalism of information field theory [9] can be used to answer these questions since it describes an inference problem by means of probabilities, which naturally permit the treatment of uncertainties. The consideration of the whole continuous phase space of possible signal configurations gives rise to the concept of a field theory instead of classical stochastic theory with a finite number of degrees of freedom.

Since we want to infer a signal from a given set of data, the so called posterior that describes the corresponding probability distribution of the signal given the data is the key element of our inference. This posterior is accessible through Bayes' theorem as a properly normalized conjunction of a likelihood and a prior. The likelihood summarizes an appropriate probabilistic model for obtaining the data from a given signal, whereas the prior is a probability distribution of the signal that describes an ignorant state of knowledge without data.

Although this terminology already implies the chronology of inference, since we want to infer from an "a priori" state of knowledge to an "a posteriori" one given some information, a more formal derivation of the reasoning process will be given at a later point. For now the implications shall be illustrated with an example concerning the aforementioned accordance of theory and experiment.

We assume to be aware of the physics behind the behavior of object in free-fall but lack the knowledge about the exact gravitational acceleration. We would like to infer its value from experimental data that lists drop heights and drop times, as well as their uncertainties, for several trails. The corresponding posterior would tell us how probable a particular gravitational acceleration would be given the data. The likelihood is rather trivial, since given a concrete value for the gravitational acceleration, it is easy to judge the plausibilities of different data points considering their uncertainties. We also have to formulate our a priori knowledge on the gravitational acceleration. On the one hand, a uniform prior would express a complete lack of knowledge, i.e. we consider all possible values equally probable. On the other hand, we may formulate a more specific prior, since we know at least that the gravitational acceleration is positive and of a finite value. With the correct normalization computed, we derive the posterior. Thus, we can

ask for the posterior mean and variance in order to find the most reasonable value for the gravitational acceleration and its uncertainty given this particular data set. If more and more data becomes available, the uncertainties shrink, the influence of our prior assumptions diminish and our estimate for the exact gravitational acceleration improves.

In general, inference deals with three fundamental problems: hypothesis testing, model selection and parameter estimation. All three are inverse problems where a given set of data needs interpretation. The problems in this thesis address the last of the three, the search for the most reasonable signal in order to explain the data at hand.

The main purpose of this thesis is to solve the inference problem of the photon flux as it is observed in high energy astronomy, i.e. the reconstruction of the spatial distribution of the photon flux and its separation into diffuse and point source contributions. Note that the diffuse and the point-like signals are entangled in data space. The loss of faint sources or small-scale structures in the reconstructed image, or the occurrence of imaging artifacts can arise due to a flawed signal estimation method. Thus, a suitable formalism should incorporate the diffuse and the point-like signals as well as their correlated uncertainties. These requirements are met by information field theory which allows for the appropriate and simultaneous treatment of signal fields and their uncertainties.

In the framework of information field theory the posterior mean field describing the expected signal configuration given the data and the corresponding covariant uncertainty information are of particular interest. Since a signal is interpreted as a field that is discretized for convenience, the covariance that encodes the underlying correlation structure of the signal is given in its matrix representation. The diagonal of such a covariance matrix is of special importance since it expresses the componentwise variance that provides an estimate of the uncertainty of the result.

In practice, it is seldom computationally feasible to state such matrices explicitly due to their high dimensionality. They are usually accessible in the form of computer routines that read in a vector and return the matrix-vector-product. Estimates for matrix diagonals are obtained by existing schemes from sample averages over multiplications with selected test vectors [17]. However, statistical inference on such samples can improve the stochastic estimates by exploiting additional knowledge in cases where some form of continuity of the solution can be assumed [27]. Since our signal inference scheme requires the computation of matrix diagonals, the application of inference methods to the estimation of diagonal entries of a matrix is investigated in this thesis as well.

Information field theory provides, among others, the technique of thermodynamical inference [10], where the inference problem is reformulated as a minimization problem in terms of a thermodynamical potential. The thermodynamical

cal inference solution emerges from a balanced mixture of two common methods, namely the maximum a posteriori and the maximum entropy methods [18, 19]. These methods derive from intuitive postulates about reasoning on the basis of probabilities which in turn derive from logic [7], the basis of all science.

1.2. Structure of this thesis

Following this introduction, we review information field theory in Sect. 2. First of all the framework of probability theory is derived, starting from Aristotelian logic. The proper definition of an information field and the consequent calculus are followed by the description of thermodynamical inference. The section concludes with a generalized application in the form of a derivation of generic filter formulas.

In Sect. 3. the improvement of stochastic estimates with inference methods for matrix diagonals is addressed. We highlight the importance of obtaining estimates for matrix diagonals, in particular of uncertainty covariance matrices in the framework of information theory. Then, the problem of their calculation in high-dimensional cases is discussed and the frequentist approach called probing, which is completely general and can be applied to all kinds of matrices, is reviewed. Subsequently, information field theory is applied to introduce a Bayesian estimate for matrix diagonals. The developed algorithm focuses on covariance matrices, which are positive and symmetric by definition, and in practice often have sparse off-diagonal entries or at least off-diagonal entries that are decaying with distance from the diagonal. A subsection is devoted to the verification and application of both methods, where we investigate simple mock examples as well as a real example: the uncertainty covariance matrix of the all sky Faraday depth derived from the NVSS catalog. A conclusion on the improvement of stochastic estimates with inference methods can be found at the end of the section.

The reconstruction and separation of the photon flux is discussed in Sect. 4., where at first the problem concerning the superposition of diffuse and point-like signals and the Poisson process behind photon counts are outlined. Afterwards a data model is set up to incorporate local shot noise, possible signal responses and a priori assumptions on the signals. Applying the Gibbs free energy formalism, a self-consistent solution of the full inverse problem is derived and a solver is introduced that uses a gradient approach in the combined phase space of all degrees of freedom. Subsequently, we discuss the results from an application to simulated data and draw a comparison to the outcomes of a standard technique that is also used as a pre-analysis in the inference. Finally, a conclusion concerning the application of thermodynamical inference to morphological component separation in high energy astronomy follows.

In Sect. 5. a conclusive summary of this thesis as well as an outlook concerning future improvements can be found.

A clarification of the used notation, definitions of the spherical harmonics, implications of statistical isotropy, and correction terms of the separation problem are discussed in the corresponding appendices.

2. Information field theory

2.1. Logic, Probabilities & Bayesics

The very foundation stone for today's dealing with probabilities has been laid by Aristotle. History teaches that he was one of the firsts to discuss the logic of propositions and their combinatorics. In the modern Boolean formulation [4] propositions a and b have truth values that can either be *true* or *false*. There are two basic combinations, the conjunction *AND*, “ \wedge ”, and the disjunction *OR*, “ \vee ”. Both can be expressed mathematically to be a logical product or sum, respectively,

$$a \wedge b = a \cdot b, \tag{1}$$

$$a \vee b = a + b. \tag{2}$$

Furthermore, the logical equality, “ $=$ ”, for the same truth values, and negation, e.g. *NOT* $a = \bar{a}$, are introduced. The Boolean algebra that is associated with the combinatorics reads as listed in Tab. 1. It has been proven that any logical function can be expressed using this algebra.

The next step would be to extend logic to plausibility, i.e. to reason the credibility of a proposition under a given hypothesis. This conditioning of the proposition b given the hypothesis a is indicated by “ $b|a$ ”. The introduction of a reasonable measure of plausibility seems in order. Let the arbitrary function $p(b|a)$, that is not yet to be associated with the term probability, be the plausibility of b given a is true. This function is insofar arbitrary as there are a number of conceivable measures. In order to give meaning to the measure of plausibility the Cox axioms [7] are postulated. First,

$$p(\bar{b}|a) = f(p(b|a)) \tag{3}$$

expresses that the plausibility values of b and \bar{b} , both under the hypothesis a , are related by a single function f that is independent of a and b . Second,

$$p(c \cdot b|a) = g(p(c|b \cdot a), p(b|a)) \tag{4}$$

manifests the intuitive assumption that the plausibilities of a conjunction can be decomposed into more elementary plausibilities using another function g that describes how these have to be combined to form the original conjunction. It can be shown that the functions f and g can be determined uniquely. According to the Cox axioms the measure p can then be defined in the interval $[0, 1]$ or $[1, \infty]$.¹

¹However, plausibilities and probabilities correspond not uniquely to each other, since plausibilities can be consistently raised to any power w in consistence with the Cox axioms. The value of the power w is merely set by convention, the common choice is $w = 1$, in the sense that

Idempotence:	$a \cdot a = a$	$a + a = a$
Double negation:		$\bar{\bar{a}} = a$
Commutativity:	$a \cdot b = b \cdot a$	$a + b = b + a$
Associativity:	$(a \cdot b) \cdot c = a \cdot (b \cdot c)$	$(a + b) + c = a + (b + c)$
Distributivity:	$a \cdot (b + c) = a \cdot b + a \cdot c$	$a + (b \cdot c) = (a + b) \cdot (a + c)$
De Morgan's law:	$\overline{(a \cdot c)} = \bar{a} + \bar{c}$	$\overline{(a + c)} = \bar{a} \cdot \bar{c}$
Absorption:	$a \cdot (a + b) = a$	$a + (a \cdot b) = a$

 Table 1: Boolean algebra for propositions a , b and c .

The former then describes plausibilities, i.e. 0 equals impossibility and 1 certainty, and the latter ‘implausibilities’ instead. The common choice is the former and leads to a measure of plausibilities which are from now on called *probabilities*. Probability distributions² are denoted by $P(\cdot)$. Note that the intuitive transitivity of plausibilities, i.e. if a is more plausible than b and b more than c it follows that a is more plausible than c , is now consistently expressed by larger probability values.

In this thesis the term probability is interpreted as a *degree of rational belief* or *objective strength of an argument*. However, there are alternative interpretations of which one understands probability as a *frequency of outcomes* in an ensemble. The physical and philosophical dispute between those schools of thinking exceeds the scope of this thesis.

The reevaluation of the Cox axioms under the assignment of probabilities to the propositions provides the sum rule,

$$P(b|a) + P(\bar{b}|a) = 1, \quad (5)$$

and the product rule,

$$P(c, b|a) = P(c|b, a)P(b|a) = P(b|c, a)P(c|a), \quad (6)$$

where the conjunction is replaced by a comma for convenience. In Eq. (6) the hypothesis a is considered to be given and thus is not questioned. Such hypothesis are often dropped in the notation for convenience and understood as being part of the underlying model. Furthermore, those rules answer the central question of probabilistic reasoning, how to judge a statement b given some fact a . Rewriting

the sum rule for two excluding propositions a and b reads $P(a + b) = P(a) + P(b)$ instead of $p^w(a + b) = p^w(a) + p^w(b)$.

²All statements that have been or will be derived for probability distributions apply for probability density functions as well. Therefore, both are used synonymous and no extra notation is introduced.

the product rule yields

$$P(b|a) = \frac{P(a, b)}{P(a)} = \frac{P(a|b)P(b)}{P(a)}, \quad (7)$$

the so called *Bayes' theorem*, that was explicitly formulated by Laplace. Due to the wide use of the Bayes' theorem a terminology has evolved: The probability $P(b|a)$ is called the *posterior*, $P(a, b)$ the *joint probability*, $P(a|b)$ the *likelihood*, $P(a)$ the *evidence*, and $P(b)$ the *prior*. This nomenclature elucidates the way of reasoning, since one wants to infer from an “a priori” state of knowledge to an “a posteriori” one, chronologically spoken. The posterior distribution that depends on all available knowledge a shall be inferred. This inference takes the joint probability $P(a, b)$, that describes the probability of both, a and b , being true at the same time, as a basis. The evidence serves merely as a normalization constant because, since it is independent of b . It is the result of a *marginalization* of the joint probability with respect to the proposition b ,

$$P(a) = \sum_i P(a, b_i) = P(a, b) + P(a, \bar{b}). \quad (8)$$

This can be proven by applying the sum rule. The technique of marginalizing is a useful tool to eliminate unknown nuisance parameters from the inference problem. But marginalized quantities are not ‘lost’, they are inherent in the model since all configurations of these parameters are summed over.

Further, the joint probability can be decomposed into the likelihood and the prior. The likelihood $P(a|b)$ describes the scenario of a given b , the inverse in comparison to the posterior. In practice, the likelihood is often easily accessible. However, the prior $P(b)$ is of a more subtle nature, since it encodes the a priori knowledge about the questioned proposition b . One fundamental class of priors are the uniform ones describing equal probabilities for all realizations in the domain. Uniform priors are often called uninformative or Jeffreys' prior [24]. Following Laplace's rule of succession, such priors should especially be applied in the case of a complete lack of knowledge concerning real-valued parameters, although for a strictly positive parameter the uniformity might apply for the logarithm of the parameter. On the other hand the choice of an ‘informative’ prior with a very specific form can be reasonable, e.g. in a physical context. There might be physical constraints on a parameter that have been proven, or physical models allow predictions on the parameter distribution. Nevertheless, the influence of any prior assumptions diminishes with an increasing amount of available information, i.e. when more and more data are provided.

2.2. Information & fields

Information is an imperative force on rational beliefs [5, 6]: A state of knowledge is expressed by the assignment of probabilities to all relevant propositions allowing for a rating between them. As soon as new information becomes available, a rational mind has to reassign the probabilities.

Moreover, information is thus far ‘physical’ as it is directly associated with a physical system, i.e. a system ‘contains’ or ‘carries’ information on physical quantities and an appropriate measurement on such a system reveals that information. Unfortunately, physical and technological limitations often prohibit a direct measurement of the physical quantity of interest for practical reasons. This motivates the search for techniques to infer information from a given state of knowledge based on a finite amount of data.

Information on physical quantities of interest can often be regarded as fields on a continuous space Ω . In this thesis we merely consider scalar fields on a unit sphere. Let $\varphi(\tilde{x})$ be such a field and \tilde{x} an element of Ω . Even if φ is continuous in a physical sense, measurements and computations alike do not permit infinite resolution. Therefore, a discretization of the continuous space Ω into pairwise disjoint, proper subsets Ω_x indexed by $x \in \{1, \dots, r\}$ is convenient. This means for the field,

$$(\varphi)_x = \varphi_x = \int_{\tilde{x} \in \Omega_x} d\tilde{x} \varphi(\tilde{x}), \quad (9)$$

where the index x denotes the discretized coordinate, i.e. a ‘pixel’, ‘grid point’, ‘bin’ or ‘voxel’. The *information field* φ can be treated as an element of some vector space whose dimension equals the number of pixels. Subtle implications of this notation can be found in App. A.

In order to illustrate the resulting handling of and calculus behind information field theory (IFT) we investigate a simple example. Let the distribution of a scalar quantity ϕ be a zero-mean Gaussian with variance σ^2 ,

$$P(\phi|\sigma^2) = \mathcal{G}(\phi, \sigma^2) = \frac{1}{\sqrt{2\pi\sigma^2}} \exp\left(-\frac{1}{2}\sigma^{-2}\phi^2\right). \quad (10)$$

The analog in IFT is a multi-dimensional Gaussian,

$$P(\varphi|\mathbf{X}) = \mathcal{G}(\varphi, \mathbf{X}) = \frac{1}{\sqrt{\det[2\pi\mathbf{X}]}} \exp\left(-\frac{1}{2}\varphi^\top \mathbf{X}^{-1} \varphi\right), \quad (11)$$

where \mathbf{X} is the covariance matrix of φ , and $^\top$ denotes transposition. The properties of a probability distribution are described by its *moments* or *n*-point functions,

i.e. for the considered scalar case,

$$\langle \phi \rangle_{(\phi|\sigma^2)} = \int d\phi \phi^1 \mathcal{G}(\phi, \sigma^2) = 0, \quad (12)$$

$$\langle \phi^2 \rangle_{(\phi|\sigma^2)} = \int d\phi \phi^2 \mathcal{G}(\phi, \sigma^2) = \sigma^2. \quad (13)$$

The generalization for IFT is analogous but the evaluation of the expectation values more tricky.

First, one needs to perform an integral over the whole phase space volume of the field φ in order to take all possible field configurations into account. The resulting phase space integral is called a path integral,

$$\prod_x \int d\varphi_x = \int \mathcal{D}\varphi. \quad (14)$$

The formalism of path integrals has been developed and established within quantum field theory, a fact IFT benefits from.

Second, the introduction of a moment generating *source function* \mathbf{J} is a convenient way of analytical treatment. The first moment then reads,

$$\begin{aligned} \langle \varphi \rangle_{(\varphi|\mathbf{X})} &= \int \mathcal{D}\varphi \varphi \mathcal{G}(\varphi, \mathbf{X}) \exp(\mathbf{J}^\top \varphi) \Big|_{\mathbf{J}=\mathbf{0}} \\ &= \frac{1}{\sqrt{\det[2\pi\mathbf{X}]}} \frac{\partial}{\partial \mathbf{J}} \int \mathcal{D}\varphi \exp\left(-\frac{1}{2}\varphi^\top \mathbf{X}^{-1} \varphi + \mathbf{J}^\top \varphi\right) \Big|_{\mathbf{J}=\mathbf{0}} \\ &= \frac{\partial}{\partial \mathbf{J}} \exp\left(\frac{1}{2}\mathbf{J}^\top \mathbf{X} \mathbf{J}\right) \Big|_{\mathbf{J}=\mathbf{0}} = \mathbf{0}. \end{aligned} \quad (15)$$

This confirms the zero-mean of the chosen Gaussian. In the same way the second moment can be evaluated,

$$\begin{aligned} \langle \varphi \varphi^\top \rangle_{(\varphi|\mathbf{X})} &= \int \mathcal{D}\varphi \varphi \varphi^\top \mathcal{G}(\varphi, \mathbf{X}) \exp(\mathbf{J}^\top \varphi) \Big|_{\mathbf{J}=\mathbf{0}} \\ &= \frac{\partial^2}{\partial \mathbf{J} \partial \mathbf{J}^\top} \exp\left(\frac{1}{2}\mathbf{J}^\top \mathbf{X} \mathbf{J}\right) \Big|_{\mathbf{J}=\mathbf{0}} = \mathbf{X}. \end{aligned} \quad (16)$$

The covariance matrix \mathbf{X} , which is positive and symmetric by definition, inherits the pairwise correlation structure of the components of φ . The diagonal entries of the covariance matrix are associated with the squared standard deviation σ_x of

the field value in the pixel x expressing the pixelwise uncertainty in $\boldsymbol{\varphi}$,

$$\langle \varphi_x^2 \rangle_{(\boldsymbol{\varphi}|\mathbf{X})} = X_{xx} = \sigma_x^2. \quad (17)$$

If \mathbf{X} were a diagonal matrix the Gaussian would be factorizable into one-dimensional Gaussians for each component of $\boldsymbol{\varphi}$,

$$\mathcal{G}(\boldsymbol{\varphi}, \mathbf{X}) = \prod_x \mathcal{G}(\varphi_x, X_{xx}). \quad (18)$$

However, this is seldom the case in practice, although covariance matrices often have sparse off-diagonal entries or at least off-diagonal entries that are decaying with distance from the diagonal.

In line with Enßlin et al. [9], the techniques described here form the basic tools for IFT. With them at hand we can start a closer investigation of potential inference algorithms.

2.3. Thermodynamical inference

One fundamental problem in Bayesian inference is parameter estimation. This kind of inverse problem deals with the search for parameter estimates in order to explain existing information under a certain model assumption.

Throughout this thesis the aim is to find a map \mathbf{m} as an estimate for the signal \mathbf{s} that has caused the observed data \mathbf{d} , and the uncertainty of this estimate. The experimenter, who provides the data, usually knows about all the relevant aspects of the detection, if only up to a certain degree of precision. The process of observation, or data acquisition in general, is usually well described and can be assumed to be understood, whereas the inverse process of deducing the signal from the data is usually nontrivial. The inference proceeds from the posterior distribution of the signal given some data set,

$$P(\mathbf{s}|\mathbf{d}) = \frac{P(\mathbf{d}, \mathbf{s})}{P(\mathbf{d})} = \frac{\exp(-H(\mathbf{d}, \mathbf{s}))}{Z(\mathbf{d})}. \quad (19)$$

Here, we introduced the *information Hamiltonian* [9]

$$H(\mathbf{d}, \mathbf{s}) = -\log P(\mathbf{d}, \mathbf{s}), \quad (20)$$

and the *partition function* $Z(\mathbf{d}) = \int \mathcal{D}\mathbf{s} P(\mathbf{d}, \mathbf{s}) = P(\mathbf{d})$ which acts as a normalization. The inclusion of a generating source function \mathbf{J} in the partition sum $Z(\mathbf{d}, \mathbf{J}) = \int \mathcal{D}\mathbf{s} P(\mathbf{d}, \mathbf{s}) \exp(\mathbf{J}^\top \mathbf{s})$ allows one to derive a general expression for all

moments $\langle \cdot \rangle$ or *cumulants* $\langle \cdot \rangle^c$, respectively³,

$$\langle s_{x_1} \cdots s_{x_n} \rangle_{(\mathbf{s}|\mathbf{d})} = \frac{1}{Z(\mathbf{d})} \left. \frac{\partial^n Z(\mathbf{d}, \mathbf{J})}{\partial J_{x_1} \cdots \partial J_{x_n}} \right|_{\mathbf{J}=\mathbf{0}}, \quad (21)$$

$$\langle s_{x_1} \cdots s_{x_n} \rangle_{(\mathbf{s}|\mathbf{d})}^c = \left. \frac{\partial^n \log Z(\mathbf{d}, \mathbf{J})}{\partial J_{x_1} \cdots \partial J_{x_n}} \right|_{\mathbf{J}=\mathbf{0}}. \quad (22)$$

The formulation of the posterior in terms of statistical mechanics suggests the transformation of the inverse problem into a search for an energetic extremum. Which quantity is the most reasonable one to be extremized is investigated in the following.

2.3.1. Maximum a posteriori

An intuitive approach would be to maximize the posterior with respect to the signal. This goes hand in hand with minimizing the Hamiltonian. However, it can be shown that the resulting *maximum a posteriori* (MAP) field \mathbf{m}^{MAP} merely optimizes the statistical L^0 -norm,

$$\mathbf{m}^{\text{MAP}} = \underset{\mathbf{s}'}{\operatorname{argmax}} P(\mathbf{s}'|\mathbf{d}) = \underset{\mathbf{s}'}{\operatorname{argmin}} \langle -\delta(\mathbf{s} - \mathbf{s}') \rangle_{(\mathbf{s}|\mathbf{d})}, \quad (23)$$

where $\delta(\cdot)$ denotes the multi-dimensional Dirac delta distribution. A superior solution would be the minimum mean square error (MMSE) estimator which optimizes the posterior in the sense of the statistical L^2 -norm. This map \mathbf{m} , still to be determined, describes the posterior mean field,

$$\mathbf{m} = \underset{\mathbf{s}'}{\operatorname{argmin}} \langle (\mathbf{s} - \mathbf{s}')^\top (\mathbf{s} - \mathbf{s}') \rangle_{(\mathbf{s}|\mathbf{d})} = \langle \mathbf{s} \rangle_{(\mathbf{s}|\mathbf{d})} = \int \mathcal{D}\mathbf{s} \, \mathbf{s} P(\mathbf{s}|\mathbf{d}). \quad (24)$$

The reason for the successful application of the MAP estimate is that the L^0 - and L^2 -norm draw near for posteriors with a Gaussian shape. In such cases \mathbf{m}^{MAP} yields a good approximation, but in other cases it may perform poorly, as e.g. illustrated in Enßlin & Frommert [8] in comparison with other estimates.

In order to obtain additional uncertainty information in the case of a Gaussian-like posterior, where one has $\mathbf{m}^{\text{MAP}} \approx \mathbf{m}$, one can consult the Hessian of the

³Moments and cumulants provide an alternative but equivalent description of a distribution. The complete set of one up to some order of \mathbf{s} can be derived from the complete set of the other up to the same order of \mathbf{s} .

Hamiltonian at its minimum,

$$\begin{aligned} \left(\frac{\delta^2 H(\mathbf{d}, \mathbf{s})}{\delta \mathbf{s} \delta \mathbf{s}^\top} \right)^{-1} \Big|_{\mathbf{s}=\mathbf{m}^{(\text{MAP})}} &= \left\langle (\mathbf{s} - \mathbf{m}^{(\text{MAP})}) (\mathbf{s} - \mathbf{m}^{(\text{MAP})})^\top \right\rangle_{(\mathbf{s}|\mathbf{d})} \\ &\approx \langle (\mathbf{s} - \mathbf{m}) (\mathbf{s} - \mathbf{m})^\top \rangle_{(\mathbf{s}|\mathbf{d})} = \mathbf{D}. \end{aligned} \quad (25)$$

The Hessian then approximates the Gaussian's covariance and thus yields an approximation for the posterior

$$P(\mathbf{s}|\mathbf{d}) \approx \tilde{P}(\mathbf{s}|\mathbf{m}, \mathbf{D}) = \mathcal{G}(\mathbf{s} - \mathbf{m}, \mathbf{D}). \quad (26)$$

In summary, it can be stated that the MAP estimation does in general not result in the wanted mean field solution but serves as a good approximation in case the posterior is close to a Gaussian.

The internal energy U is a thermodynamic potential that is related to the Hamiltonian. In the IFT framework it is defined as the posterior expectation of the Hamiltonian, i.e. in the Gaussian approximation,

$$U = \langle H(\mathbf{d}, \mathbf{s}) \rangle_{(\mathbf{s}|\mathbf{d})} \approx \langle H(\mathbf{d}, \mathbf{s}) \rangle_{(\mathbf{s}|\mathbf{m}, \mathbf{D})} = \tilde{U}(\mathbf{d}, \mathbf{m}, \mathbf{D}). \quad (27)$$

Ergo, the minimization of the internal energy with respect to all its degrees of freedom, i.e. \mathbf{m} and for uncertainty information also \mathbf{D} , leads to a MAP solution of the modified posterior that might be reasonable in cases where the original posterior is of a Gaussian shape.

2.3.2. Maximum entropy

Another noteworthy method is the *maximum entropy* (ME) principle introduced in Jaynes [18, 19]. The entropy is there introduced as an ordering scheme for the functional forms probabilities can take in a way that the most appropriate one, describing the knowledge state most accurately, is defined as having maximum entropy. In the reviews Caticha [5, 6] a general concept of such an entropy is derived by three fundamental criteria: locality, coordinate invariance and system independence – i.e. first, information on a subdomain affects the state of knowledge only inside this subdomain. Second, the coordinates do not carry any information themselves. Third, the separate or joint treatment of independent systems makes no difference.

It can be shown that as a consequence of these criteria the *information entropy* is, up to irrelevant constants, uniquely determined and reads in the accustomed

notation,

$$S_E[P, Q] = - \int \mathcal{D}\mathbf{s} P(\mathbf{s}|\mathbf{d}) \log \frac{P(\mathbf{s}|\mathbf{d})}{Q(\mathbf{s})}. \quad (28)$$

$Q(\mathbf{s})$ denotes a prior that expresses the maximally ignorant state of knowledge. When new information becomes available, one wants to update from this “a priori” state to an “a posteriori” one that is still most ignorant but consistent with the prior and the data. This updating to the most minimal extent that is required by the constraints of both, the prior and the data, is called the principle of minimal updating [6].

The maximum entropy principle becomes more obvious when considering the *Kullback-Leibler-divergence* [20]. This asymmetric measure is defined as

$$d_{\text{KL}}[\tilde{P}; P] = \int \mathcal{D}\mathbf{s} \tilde{P}(\mathbf{s}) \log \frac{\tilde{P}(\mathbf{s})}{P(\mathbf{s})}, \quad (29)$$

and describes the information theoretical distance between two probability density functions (PDFs). The negative of this measure quantifies the *cross information*. It is evident that $S_E[P, Q] = -d_{\text{KL}}[P; Q]$, i.e. the higher the entropy, the larger the cross information between prior and posterior.

Thus, a set of conceivable posteriors can be rated by the information entropy S_E with due regard to the constraints. However, the maximum entropy principle alone does not provide an algorithm, since it merely singles out a posterior PDF according to the principle of minimal updating.

In thermodynamics the *Boltzmann entropy*⁴ for the posterior reads,

$$S_B[P] = - \int \mathcal{D}\mathbf{s} P(\mathbf{s}|\mathbf{d}) \log P(\mathbf{s}|\mathbf{d}) = \langle -\log P(\mathbf{s}|\mathbf{d}) \rangle_{(\mathbf{s}|\mathbf{d})}, \quad (30)$$

where in comparison to Eq. (28) a uniform prior $Q(\mathbf{s}) \equiv 1$ is already implied. Therefore, S_B singles out the posterior that is most ignorant but complies with the constraints of the available data.

With the insights from Sect. 2.3.1. an investigation of the Gibbs free energy which combines internal energy and Boltzmann entropy seems in order.

2.3.3. Minimum Gibbs free energy

For a full thermodynamic treatment the *temperature* T and again a source function \mathbf{J} are introduced in order to complete the pairs of conjugate variables (S_B, T) and

⁴Here, stated in Shannon’s formulation for PDFs.

(\mathbf{m}, \mathbf{J}) .⁵ The signal posterior stated in Eq. (19) needs therefore to be ‘tempered’,

$$P(\mathbf{s}|\mathbf{d}, \mathbf{J}, T) = \frac{(P(\mathbf{d}, \mathbf{s}) \exp(-\mathbf{J}^\top \mathbf{m}))^\beta}{\int \mathcal{D}\mathbf{s}' (P(\mathbf{d}, \mathbf{s}') \exp(-\mathbf{J}^\top \mathbf{s}'))^\beta} = \frac{\exp(-\beta (H(\mathbf{d}, \mathbf{s}) + \mathbf{J}^\top \mathbf{s}))}{Z(\mathbf{d}, \mathbf{J}, T)}, \quad (31)$$

where $\beta = 1/T$ stands for the inverse temperature as usual. The significance of the temperature in Eq. (31) becomes clearer considering the following three relevant cases: $T = 1$ preserves the original posterior, while $T < 1$ narrows it until it converges for $T \rightarrow 0$ to a delta peak at the posterior maximum, i.e. yields the MAP solution. Moreover, the tempered posterior broadens for $T > 1$ and for $T \rightarrow \infty$ becomes uniform, i.e. the posterior describes an unconstrained ME state. The temperature specifies how much the resulting inference method singles out a solution close to the MAP or the ME solution.

A suitable algorithm should yield a map \mathbf{m} and the according uncertainties in form of the covariance matrix \mathbf{D} . For that reason, and the fact that analytical manageability is preferred, it is often sufficient to restrict the modified posterior to a Gaussian [10],

$$P(\mathbf{s}|\mathbf{d}, \mathbf{J}, T) \approx \tilde{P}(\mathbf{s}|\mathbf{m}, \mathbf{D}) = \mathcal{G}(\mathbf{s} - \mathbf{m}, \mathbf{D}). \quad (32)$$

This approximation is considered for all further derivation. Up to now it still holds that $\mathbf{m} = \mathbf{m}(\mathbf{d}, \mathbf{J}, T)$ and $\mathbf{D} = \mathbf{D}(\mathbf{d}, \mathbf{J}, T)$. As a consequence of the posterior tempering also the internal energy U and the entropy S_B are modified. Following Eq. (27) the internal energy then reads,

$$U(\mathbf{d}, \mathbf{J}, T) = \langle H(\mathbf{d}, \mathbf{s}) \rangle_{(\mathbf{s}|\mathbf{d}, \mathbf{J}, T)} \approx \langle H(\mathbf{d}, \mathbf{s}) \rangle_{(\mathbf{s}|\mathbf{m}, \mathbf{D})} = \tilde{U}(\mathbf{d}, \mathbf{m}, \mathbf{D}). \quad (33)$$

The definition of the Boltzmann entropy yields in the Gaussian approximation,

$$\begin{aligned} S_B &= - \int \mathcal{D}\mathbf{s} P(\mathbf{s}|\mathbf{d}, \mathbf{J}, T) \log P(\mathbf{s}|\mathbf{d}, \mathbf{J}, T) \\ &\approx - \int \mathcal{D}\mathbf{s} \tilde{P}(\mathbf{s}|\mathbf{m}, \mathbf{D}) \log \tilde{P}(\mathbf{s}|\mathbf{m}, \mathbf{D}) \\ &= - \int \mathcal{D}\mathbf{s} \mathcal{G}(\mathbf{s} - \mathbf{m}, \mathbf{D}) \log \mathcal{G}(\mathbf{s} - \mathbf{m}, \mathbf{D}) = \frac{1}{2} \text{tr} [\mathbb{1} + \log(2\pi \mathbf{D})] = \tilde{S}_B(\mathbf{D}). \end{aligned} \quad (34)$$

Note that within this approximation the Boltzmann entropy is a function only of the covariance matrix \mathbf{D} . Alternatively to Eq. (34), the entropy can be expressed

⁵A third pair including the data \mathbf{d} is not needed since \mathbf{d} is considered to be given.

by thermodynamical potentials,

$$S_B = \langle -\log P(\mathbf{s}|\mathbf{d}, \mathbf{J}, T) \rangle_{(\mathbf{s}|\mathbf{d}, \mathbf{J}, T)} \approx \beta \left(\tilde{U} + \mathbf{J}^\top \mathbf{m} - F \right), \quad (35)$$

where F denotes the Helmholtz free energy,

$$F(\mathbf{d}, \mathbf{J}, T) = -T \log Z(\mathbf{d}, \mathbf{J}, T) \approx \tilde{U}(\mathbf{d}, \mathbf{m}, \mathbf{D}) - T\tilde{S}_B(\mathbf{D}) + \mathbf{J}^\top \mathbf{m}. \quad (36)$$

According to Eq. (22) the \mathbf{J} -dependent Helmholtz free energy provides all cumulants of the original posterior PDF for $T = 1$,

$$\langle s_{x_1} \cdots s_{x_n} \rangle_{(\mathbf{s}|\mathbf{d})}^c = \left. \frac{\partial^n F(\mathbf{d}, \mathbf{J}, T)}{\partial J_{x_1} \cdots \partial J_{x_n}} \right|_{\mathbf{J}=\mathbf{0}, T=1}. \quad (37)$$

For the purpose of eliminating the explicit \mathbf{J} dependence a Legendre transformation is performed with respect to \mathbf{J} yielding the Gibbs free energy

$$G(\mathbf{d}, \mathbf{m}, T) = F(\mathbf{d}, \mathbf{J}, T) - \mathbf{J}^\top \frac{\partial}{\partial \mathbf{J}} F(\mathbf{d}, \mathbf{J}, T), \quad (38)$$

where $\mathbf{J} = \mathbf{J}(\mathbf{m})$ is assumed on the right-hand side to be given by the inverse $\mathbf{m}(\mathbf{J})$, as it is defined by $\mathbf{m} = \langle \mathbf{s} \rangle_{(\mathbf{s}|\mathbf{d})}$ in Eq. (15) for $\mathbf{J} \neq \mathbf{0}$.

In the considered Gaussian approximation, where the data \mathbf{d} are given and the temperature T is fixed, the Gibbs free energy is only a function of the map \mathbf{m} and the covariance matrix \mathbf{D} ,

$$G(\mathbf{m}, \mathbf{D}) = \tilde{U}(\mathbf{m}, \mathbf{D}) - T\tilde{S}_B(\mathbf{D}). \quad (39)$$

The Gibbs free energy provides a temperature balanced mixture of the MAP and ME method. Minimizing it yields a solution of the approximated inverse problem. In case the posterior is indeed a Gaussian the choice $T = 1$ leads to the exact solution. If this is not the case one can investigate the posterior's features around its center or the asymptotic behavior by using a low or high temperature, respectively. Modeling the posterior as a combination of multiple normal distributions with different temperatures would allow for a more complete representation. This multi-temperature approach is detailed in Enßlin & Weig [10]. In conclusion, for each temperature the posterior is probed on different scales. Though the default choice is $T = 1$, the optimum depends on the concrete application. In Enßlin et al. [9] one can find an example where the choice of $T = 0.5$ outperforms both, $T = 0$ and $T = 1$.

Furthermore, at $T = 1$ the Gibbs free energy becomes effectively equivalent to

the Kullback-Leibler-divergence,

$$\begin{aligned}
 G(\mathbf{m}, \mathbf{D}) &= \left\langle H(\mathbf{d}, \mathbf{s}) \right\rangle_{(\mathbf{s}|\mathbf{m}, \mathbf{D})} + \left\langle \log \tilde{P}(\mathbf{s}|\mathbf{m}, \mathbf{D}) \right\rangle_{(\mathbf{s}|\mathbf{m}, \mathbf{D})} \\
 &= \int \mathcal{D}\mathbf{s} \tilde{P}(\mathbf{s}|\mathbf{m}, \mathbf{D}) \log \left(\frac{\tilde{P}(\mathbf{s}|\mathbf{m}, \mathbf{D})}{P(\mathbf{s}|\mathbf{d})} \right) - \underbrace{\log P(\mathbf{d})}_{\text{const.}} \\
 &= d_{\text{KL}}[\tilde{P}; P] + \text{const.}
 \end{aligned} \tag{40}$$

The evidence $P(\mathbf{d})$ can be neglected since it depends only on the data and not on any degrees of freedom of the signal. The interpretation is that a minimum Gibbs free energy at $T = 1$ goes along with maximal cross information between the original posterior and its approximation.

All in all, the minimum Gibbs free energy principle provides an inference method that combines the strategies of both, the MAP and the ME principle. This method can be described in a straightforward scheme:

1. Define the joint probability $P(\mathbf{d}, \mathbf{s})$ of the problem by means of a likelihood $P(\mathbf{d}|\mathbf{s})$ and a prior $P(\mathbf{s})$.
2. Compute the negative logarithm of the joint probability which is the information Hamiltonian, $H(\mathbf{d}, \mathbf{s}) = -\log P(\mathbf{d}, \mathbf{s})$.
3. Specify a suitable posterior model and fix a temperature, e.g. a Gaussian approximation $P(\mathbf{s}|\mathbf{d}) \approx \tilde{P}(\mathbf{s}|\mathbf{d}) = \mathcal{G}(\mathbf{s} - \mathbf{m}, \mathbf{D})$ and $T = 1$.
4. Compute the internal energy $\tilde{U} = \langle H \rangle_{\tilde{P}}$ and the entropy $\tilde{S}_B = \langle -\log \tilde{P} \rangle_{\tilde{P}}$ as expectation values weighted by the posterior approximation.
5. Minimize the Gibbs free energy $G = \tilde{U} + T\tilde{S}_B$ with respect to all degrees of freedom, and extract all quantities of interest.

The described minimum Gibbs free energy principle results in an approximated state of knowledge, that exhibits maximal cross information with the most ignorant one while still considering all available data within the chosen posterior approximation. From this state all quantities of interest, such as posterior mean and variance, can be retrieved. This method is applied to all problems addressed in this thesis.

2.4. Generic filter

2.4.1. Generalized Wiener filter

Following Enßlin et al. [9, 10] we review the generalized Wiener filter by means of the minimum Gibbs free energy principle. This filter is based on a linear forward

data model

$$\mathbf{d} = \mathbf{R} \mathbf{s} + \mathbf{n}, \quad (41)$$

where the data \mathbf{d} is a sum of signal response $\mathbf{R} \mathbf{s}$ and noise \mathbf{n} . In this scenario, the response is a linear operator that inherits all aspects of the signal detection, i.e. the detector's input-output relation⁶.

The generalized Wiener filter arises in case one can assume a Gaussian distribution for the signal's prior and the signal-independent noise in addition to the described forward data model,

$$P(\mathbf{s}) = \mathcal{G}(\mathbf{s}, \mathbf{S}), \quad (42)$$

$$P(\mathbf{n}|\mathbf{s}) = \mathcal{G}(\mathbf{n}, \mathbf{N}), \quad (43)$$

where \mathbf{S} and \mathbf{N} stand for the signal and noise covariance matrix, respectively, and are assumed to be known. Ergo, the likelihood of the data given the signal becomes

$$P(\mathbf{d}|\mathbf{s}) = P(\mathbf{n}|\mathbf{s}) = \mathcal{G}(\mathbf{d} - \mathbf{R}\mathbf{s}, \mathbf{N}). \quad (44)$$

Multiplying the prior $P(\mathbf{s})$ and the likelihood $P(\mathbf{d}|\mathbf{s})$ one obtains the joint probability and thus an expression for the information Hamiltonian

$$\begin{aligned} H(\mathbf{s}) &= -\log P(\mathbf{d}, \mathbf{s}) \\ &= H_0 - \underbrace{(\mathbf{R}^\top \mathbf{N}^{-1} \mathbf{d})^\top}_{\mathbf{j}^\top} \mathbf{s} + \frac{1}{2} \mathbf{s}^\top \underbrace{(\mathbf{S}^{-1} + \mathbf{R}^\top \mathbf{N}^{-1} \mathbf{R})}_{\mathbf{D}'^{-1}} \mathbf{s}, \end{aligned} \quad (45)$$

$$H_0 = \frac{1}{2} \mathbf{d}^\top \mathbf{N}^{-1} \mathbf{d} + \frac{1}{2} \log (\det [2\pi \mathbf{S}] \det [2\pi \mathbf{N}]), \quad (46)$$

where the terms have been reordered in powers of \mathbf{s} and all constant ones have been absorbed into H_0 for convenience. Note that the Hamiltonian is of order $\mathcal{O}(s^2)$ since both, prior and likelihood, are Gaussians. Therefore it is reasonable to approximate the posterior by a Gaussian, too. Let the posterior be

$$P(\mathbf{s}|\mathbf{d}) \approx \tilde{P}(\mathbf{s}|\mathbf{m}, \mathbf{D}) = P(\boldsymbol{\varphi}|\mathbf{D}) = \mathcal{G}(\boldsymbol{\varphi}, \mathbf{D}), \quad (47)$$

where $\boldsymbol{\varphi} = \mathbf{s} - \mathbf{m}$ and \mathbf{D} is the associated covariance matrix. Up to this point the unknown \mathbf{D} and the known \mathbf{D}' are distinct and their relation remains to be determined. The next step is to get an expression for the Gibbs free energy. For

⁶This may e.g. include the detector's point spread function, survey coverage, etc.

that the internal energy needs to be evaluated, which can be done analytically,

$$\begin{aligned}\tilde{U}(\mathbf{m}, \mathbf{D}) &= \langle H(\mathbf{s}) \rangle_{(\varphi|\mathbf{D})} \\ &= H_0 - \mathbf{j}^\top \mathbf{m} + \frac{1}{2} \mathbf{m}^\top \mathbf{D}'^{-1} \mathbf{m} + \frac{1}{2} \text{tr} [\mathbf{D} \mathbf{D}'^{-1}].\end{aligned}\quad (48)$$

The entropy for the Gaussian case is already given by Eq. (34). Therefore, the Gibbs free energy reads according to Eq. (39),

$$\begin{aligned}G(\mathbf{m}, \mathbf{D}) &= G_0 - \mathbf{j}^\top \mathbf{m} + \frac{1}{2} \mathbf{m}^\top \mathbf{D}'^{-1} \mathbf{m} + \frac{1}{2} \text{tr} [\mathbf{D} \mathbf{D}'^{-1}] - \frac{T}{2} \log(\det[\mathbf{D}]), \\ G_0 &= H_0 - \frac{T}{2} (1 + \log(2\pi)) \text{tr}[\mathbb{1}].\end{aligned}\quad (49)$$

The minimization with respect to \mathbf{m} and \mathbf{D} yields a general solution that is linear in the data,

$$\mathbf{m} = \mathbf{D}' \mathbf{j} \quad \text{and} \quad \mathbf{D} = T \mathbf{D}'.$$

For $T = 1$ the resulting filter formula of the generalized Wiener filter reads,

$$\mathbf{m} = \underbrace{(\mathbf{S}^{-1} + \mathbf{R}^\top \mathbf{N}^{-1} \mathbf{R})^{-1}}_{\mathbf{D}} \underbrace{(\mathbf{R}^\top \mathbf{N}^{-1} \mathbf{d})}_{\mathbf{j}}, \quad (50)$$

where the map \mathbf{m} is the Bayesian estimator for the signal, i.e. its posterior mean, \mathbf{D} is referred to as *information propagator* and \mathbf{j} as *information source*⁷. Furthermore, the choice of $T = 1$ is justified since the inverse problem of estimating the signal given the data leads to a Gaussian posterior,

$$P(\mathbf{s}|\mathbf{d}) = \mathcal{G}(\mathbf{s} - \mathbf{m}, \mathbf{D}), \quad (51)$$

with the mean \mathbf{m} and the covariance matrix \mathbf{D} that encodes the a posteriori signal uncertainty. Both, the signal covariance \mathbf{S} and the noise covariance \mathbf{N} , needed for this, are here assumed to be known. A convenient description of these covariances is in terms of their power spectra, the spectra of the eigenvalues of these matrices, as well as their eigenbasis in which the covariance matrices are diagonal. The power spectrum provides a full description of the 2-point-correlation structure which often exhibits smoothness on some not necessarily known spatial scales.

In the following we assume the signal \mathbf{s} to be statistically isotropic and thus decompose the signal covariance by $\mathbf{S} = \sum_l C_l \mathbf{S}_l$, where the \mathbf{S}_l are projection op-

⁷The names ‘propagator’ and ‘source’ are chosen in analogy to quantum field theory.

erators that project onto a suitable subspace of the eigen basis, the spectral bands. An analogous decomposition exists for the inverse $\mathbf{S}^{-1} = \sum_l C_l^{-1} \mathbf{S}_l^{-1}$. These decompositions in spectral parameters and projections are detailed in App. B for problems posed on the sphere as they occur throughout this thesis.

2.4.2. Lack of spectral knowledge

The signal's power spectrum might be unknown a priori, whereas the eigenbasis can often be guessed from statistical symmetries, e.g. the spherical harmonics basis in case of a statistically isotropic distribution on the sphere, see App. B. Thus, the spectral coefficients C_l allow for a parameterization of the covariance matrix. The incorporation of spectral parameters in the reconstruction allows one to exploit additional knowledge on the correlation structure.

One way to implement the lack of spectral knowledge is to introduce a spectral prior $P(C)$ as a product of independent prior distributions for each spectral parameter, cf. [8],

$$P(C) = \prod_l P(C_l), \quad (52)$$

where $P(C_l) = \mathcal{I}(C_l; \alpha_l, q_l)$ is given by the inverse-gamma distribution⁸ \mathcal{I} which describes a power-law with a negative slope α_l and an exponential cutoff q_l at low values,

$$\mathcal{I}(C_l; \alpha_l, q_l) = \frac{1}{q_l \Gamma(\alpha_l - 1)} \left(\frac{C_l}{q_l} \right)^{-\alpha_l} \exp \left(-\frac{q_l}{C_l} \right). \quad (53)$$

In case of a complete lack of spectral knowledge each spectral prior should be flat on a logarithmic scale according to Laplace's rule of succession. The inverse-gamma distribution becomes uniform on a logarithmic scale for $\alpha \rightarrow 1^+$ and $\gamma \rightarrow 0^+$. A choice of $\alpha > 1$, on the other hand, would result in an informative prior which can be used to model e.g. photon flux from point-like sources, see Sect. 4.2.4.

As a consequence of the parameterization the Hamiltonian in Eq. (45) is extended to a joint Hamiltonian $H(\mathbf{s}, C) = H(\mathbf{s}|C) + H(C)$ by a prior energy $H(C)$ of the spectral parameters,

$$H(C) = \sum_l \left(\alpha_l \log C_l + \frac{q_l}{C_l} - \log \left(\frac{q_l^{\alpha_l - 1}}{\Gamma(\alpha_l - 1)} \right) \right). \quad (54)$$

⁸This distribution is insofar the 'inverse' of the Γ -distribution as the roles of argument and cutoff parameter have been inverted.

Further energy terms encoding prior expectations on spectral smoothness are discussed in Enßlin & Frommert [8], but such approaches go beyond the scope of this thesis.

In Enßlin & Frommert [8] five different filters have been derived using different approaches and approximations, which all could be cast into a set of two self-consistent equations. These generic filter formulas are Eq. (50) complemented by a reconstruction rule for the power spectrum, i.e. for each spectral coefficient one calculates

$$C_l = \frac{1}{\varrho_l + 2\epsilon_l} \text{tr} [(\mathbf{m}\mathbf{m}^\top + \delta_l \mathbf{D}) \mathbf{S}_l^{-1}] , \quad (55)$$

where $\varrho_l = \text{tr} [\mathbf{S}_l^{-1} \mathbf{S}_l]$ are the degrees of freedom for each spectral band. A prior that is flat on a logarithmic scale has been assumed for the spectral coefficients in the derivation of this formula. The parameters (δ_l, ϵ_l) characterize the different filter options: Two specific forms are the *classical filter* for which one chooses $(\delta_l, \epsilon_l) = (0, 0)$ and the *critical filter* for which $(\delta_l, \epsilon_l) = (1, 0)$. The former can be derived from a ‘classical’ MAP approximation of the spectral uncertainty marginalized problem. The latter is called ‘critical’ because it exhibits only a marginal perception threshold in contrast to the classical filter. For a filter with a perception threshold the signal to noise ratio of a spectral mode has to exceed a certain threshold in the data before the filter recognizes it at all. There exists a critical line in the δ - ϵ -plane separating filters that fully suppress bands with insufficient spectral power from filters that do not. The critical filter resides exactly on this line while the classical filter is in the region with such a perception threshold.

All in all, Eq. (50) and (55) provide an iterative scheme for the full inverse problem of signal reconstruction with completely unknown power spectrum. The signal reconstruction benefits from this additional spectral information since it encodes the correlation structure of the signal. If in addition one lacks the a priori knowledge about the correlation structure of the noise, an analogous approach is conceivable. A correct treatment of the additionally unknown noise covariance matrices is addressed in Oppermann et al. [22].

The result of the inference is firstly a map \mathbf{m} describing the posterior mean field of the signal in order to explain the given data \mathbf{d} and secondly a covariance matrix \mathbf{D} that encodes the underlying uncertainty correlation structure. The matrix diagonal of \mathbf{D} is thereby of special importance since it expresses the pixelwise variance allowing to make a statement about the uncertainty of the result in each pixel.

The generic filter formulas are applied e.g. in [8, 10, 21, 22].

3. Estimation of a matrix diagonal

The computation of operator properties is a necessity throughout all areas of scientific computation. At the present day the majority of operators one finds in applications are linear and hence are conveniently represented as matrices in the computer environment. However, the computational complexity often prohibits an explicit representation. Instead only the operation itself, meaning the matrix-vector-multiplication, is available in form of a computer routine. A straightforward way to extract the diagonal of such a matrix would be to execute the product with every single basis vector. Unfortunately, such a procedure would be prohibitively expensive because the computational costs would scale with a higher than linear power of the dimensionality of the problem. Current problems in signal reconstruction, as they are e.g. addressed in this thesis, exhibit many degrees of freedom and thus high dimensionality.

It is a common practice in numerics to evade this by relying on stochastic approaches. The *probing* technique suggests the computation of several matrix-vector-multiplications with suitable vectors. An appropriate averaging scheme over the sample should then yield a result, but that involves stochastic errors. These residual errors decrease with increasing sample size so that one has to find an acceptable trade-off between the intended level of precision and the required computational costs.

From a physicist's point of view, such stochastic estimates describe a sort of measurement process that is of course subject to uncertainties. Ergo, inference techniques provide an alternative approach for estimators of matrix diagonals. On the one hand a sophisticated inference algorithm can exploit additional knowledge on the problem, e.g. an underlying correlation structure that does not need to be known a priori. On the other hand it has to exceed the probing estimate by means of accuracy or computational speed, respectively, to be worth implementing.

Previous work

The search for estimators of properties of matrices led to the stochastic method of probing. For this purpose the matrices are multiplied with test vectors in a way which statistically projects out the property of interest, here, the matrix diagonal. A first proposal for such a probing method can be found in the work by Hutchinson [17, and references therein]. There, the functionality and efficiency of probing for obtaining trace estimates has been proven.

Bekas et al. [2] extended the probing to Hadamard vectors⁹ to improve the estimation of diagonals of banded matrices. Those methods have been oriented to applications in density functional theory. Similar problems were approached

⁹Hadamard vectors are the rows of the Hadamard matrix.

by Tang and Saad [31] and references therein, with a focus on non-stochastic estimators.

The recent paper by Aune and Simpson [1] transfers the probing technique to the field of information theory, in particular to the calculation of log-likelihoods.

Finally, in the extensive work of Rohde and Tsybakov [25], the noise corrupted observation of unknown matrix entries is investigated from a more mathematical point of view.

3.1. Problem

Linear operators are fundamental in any area of computation and thereby often expressed in their matrix representation.

In the field of information theory the covariance matrix¹⁰ of a quantity holds a key role. Consider e.g. a multi-dimensional zero-mean Gaussian $\mathcal{G}(\boldsymbol{\varphi}, \mathbf{X})$ as given in Eq. (11). We saw already in Sect. 2.2. that the diagonal entries of the covariance matrix $\mathbf{X} = \langle \boldsymbol{\varphi} \boldsymbol{\varphi}^\top \rangle_{\mathcal{G}}$ are associated with the uncertainty map $\sqrt{\text{diag}[\mathbf{X}]}$ of the random field $\boldsymbol{\varphi}$.

Furthermore, solutions may conceivably exhibit an explicit dependence on the diagonal of the covariance matrix. This occurs even for the considered Gaussian example,

$$\langle \exp(\boldsymbol{\varphi}) \rangle_{\mathcal{G}} = \exp\left(\frac{1}{2} \hat{\mathbf{X}}\right), \quad (56)$$

where, firstly the exponent is to be understood componentwise and secondly an abbreviation of the matrix diagonal in form of an operator, $\hat{\mathbf{X}} = \text{diag}[\mathbf{X}]$, has been introduced, see App. A for notation details. Note further that the Gibbs energy derived in Sect. 4.3. exhibits several of those explicit terms. This gives reason to study applicable computation strategies and to improve them if possible.

Additional reasons are given by the generic filter formulas [8], a sophisticated and effective reconstruction tool that has been reviewed in Sect. 2.4. In order to apply the critical or other generic filters the calculation of the trace of $\mathbf{D} \mathbf{S}_l^{-1}$ in Eq. (55) in each iteration might be necessary, as well as the evaluation of the diagonal of \mathbf{D} in order to interpret the reliability of the results. This motivates our ambition to develop faster and more accurate matrix probing schemes.

3.1.1. Exact matrix diagonal

The diagonal of the uncertainty covariance \mathbf{D} is a quantity of interest, but unfortunately not directly accessible in most cases. Its calculation involves complex

¹⁰Its inverse equals the so-called precision matrix.

matrix operations such as matrix inversion, see e.g. Eq. (50). Often the complete matrix is not known explicitly, only the matrix-vector-multiplication is available in form of a computer routine which reads in and returns a vector.

Calculating the diagonal of a matrix \mathbf{X} of dimension r seems still possible using the canonical basis vectors¹¹ $\mathbf{e}^{(k)}$.

$$\hat{\mathbf{X}} = \sum_k \mathbf{e}^{(k)} * \mathbf{X} \mathbf{e}^{(k)}, \quad (57)$$

where “ $*$ ” denotes a componentwise product in the way that $(\mathbf{a} * \mathbf{b})_i = a_i b_i \forall i \in \{1, \dots, r\}$, see App. A.

It is obvious that this ‘true’ diagonal is computationally too expensive because one needs to evaluate the matrix-vector-multiplication exactly r times looping through all basis vectors where the dimension r of the problem can be very high. In addition each of those products alone can be expensive because it may invoke numerical inversion techniques, e.g. conjugate gradient [28], which is the case in most of the examples in Sect. 3.4.

3.2. Probing estimate

The question arises if one can choose another set of vectors instead of the full set of canonical basis vectors to speed up the computation. Independent and identically distributed random variables stored in a set of vectors $\{\boldsymbol{\xi}\}$ with sample size $A = |\{\boldsymbol{\xi}\}|$ work out if they fulfill the property

$$\langle \xi_i \xi_j \rangle_{\{\boldsymbol{\xi}\}} \xrightarrow{A \rightarrow \infty} \delta_{ij}. \quad (58)$$

The average $\langle \cdot \rangle_{\{\boldsymbol{\xi}\}}$ stands for the arithmetic mean over a set $\{\boldsymbol{\xi}\}$ and δ_{ij} for the Kronecker delta.

Two of many possible options are (i) equally probable values of ± 1 for the components of $\boldsymbol{\xi}$ [17]¹² or (ii) zero-mean Gaussian random numbers with unit variance. Both were originally developed for trace estimation. Option (ii) is used in the following applications.

Regardless of the choice of the random vectors, the sample average

$$\langle \boldsymbol{\xi} * \mathbf{X} \boldsymbol{\xi} \rangle_{\{\boldsymbol{\xi}\}} \xrightarrow{A \rightarrow \infty} \hat{\mathbf{X}} \quad (59)$$

over an infinite set results in the ‘true’ diagonal, see Selig et al. [27] for the formal

¹¹The canonical basis vectors $\mathbf{e}^{(k)}$ are defined as $e_i^{(k)} = \delta_{ik} \forall i, k \in \{1, \dots, r\}$ and hence form an orthonormal basis.

¹²In Bekas [2] a much more sophisticated choice, based on Hutchinson [17], is presented.

proof. The average over a finite but sufficiently large set ($A < r < \infty$) gives the probing estimator \mathbf{f} of the matrix diagonal,

$$\hat{\mathbf{X}} \approx \langle \boldsymbol{\xi} * \mathbf{X} \boldsymbol{\xi} \rangle_{\{\boldsymbol{\xi}\}} = \mathbf{f}. \quad (60)$$

Given this estimator, a trace estimate is obtained by summing up all elements of \mathbf{f} , as

$$\text{tr}[\mathbf{X}] \approx \langle \boldsymbol{\xi}^\top \mathbf{X} \boldsymbol{\xi} \rangle_{\{\boldsymbol{\xi}\}} = \sum_i f_i. \quad (61)$$

Since one wants to obtain an estimate in a finite period of time, one has to find an acceptable trade-off between the sample size A and the residual error, where the latter scales with $1/\sqrt{A}$ according to the law of large numbers. Aiming for a certain precision therefore requires a particular amount of computation time.

The estimator given by Eq. (60) is absolutely generic and applicable to a variety of matrices. Recent applications of it can be found in [2, 1, 21].

3.3. Bayesian estimate

3.3.1. Forward model

Instead of doing a blind probing, we now want to develop a Bayesian estimate which exploits additional knowledge of the problem to infer the matrix diagonal from a smaller set of samples. For this purpose the sampling described by Eq. (60) is considered as a linear forward model of a measurement process for the signal $\tilde{\mathbf{s}} = \hat{\mathbf{X}}$ of interest. In order to avoid confusion, already introduced synonymous quantities that appear now in another context are marked with a tilde.

For one sample, $a \in \{1, \dots, A\}$, the measurement equation takes the form

$$\begin{aligned} \tilde{\mathbf{d}}^{(a)} &= \boldsymbol{\xi}^{(a)} * \mathbf{X} \boldsymbol{\xi}^{(a)} \\ &= \underbrace{\text{diag} \left[\left(\xi_1^{(a)} \right)^2, \dots, \left(\xi_r^{(a)} \right)^2 \right]}_{\tilde{\mathbf{R}}^{(a)}} \tilde{\mathbf{s}} + \tilde{\mathbf{n}}^{(a)}. \end{aligned} \quad (62)$$

For all samples it is

$$\begin{aligned}
\tilde{\mathbf{d}} &= \left(\tilde{\mathbf{d}}^{(1)}, \dots, \tilde{\mathbf{d}}^{(A)} \right)^\top \\
&= \underbrace{\left(\tilde{\mathbf{R}}^{(1)}, \dots, \tilde{\mathbf{R}}^{(A)} \right)^\top}_{\tilde{\mathbf{R}}} \tilde{\mathbf{s}} + \underbrace{\left(\tilde{\mathbf{n}}^{(1)}, \dots, \tilde{\mathbf{n}}^{(A)} \right)^\top}_{\tilde{\mathbf{n}}} \\
&= \tilde{\mathbf{R}} \tilde{\mathbf{s}} + \tilde{\mathbf{n}},
\end{aligned} \tag{63}$$

where $\tilde{\mathbf{d}}$ represents the ‘measured’ data, $\tilde{\mathbf{R}}$ the response, and $\tilde{\mathbf{n}}$ the noise. The contributions from all off-diagonal matrix elements are considered to be noise, i.e.

$$\tilde{\mathbf{n}}^{(a)} = \boldsymbol{\xi}^{(a)} * \left(\mathbf{X} - \hat{\mathbf{X}} \right) \boldsymbol{\xi}^{(a)}. \tag{64}$$

The noise can be estimated using Eq. (63), once an estimator for the signal has been obtained.

Note that if one chooses the random variables ξ to be ± 1 , firstly one does not have to evaluate normal variables as originally pointed out in Hutchinson [17] and secondly all the response matrices $\mathbf{R}^{(a)}$ equal $\mathbf{1}$ and hence do not need to be treated separately for the different samples. This speeds up the algorithm and reduces the memory requirements.

3.3.2. Inference algorithm

The goal is to find an estimator for the matrix diagonal which is close to the MMSE, but still computationally affordable. This estimator has to account for the missing knowledge about the underlying correlation structure. Given these requirements the generic filter formulas are potentially an appropriate choice. Therefore, the proposed inference algorithm is based on this filter.

We start by probing the matrix as described in Sect. 3.2. and as a result obtain a first estimator \mathbf{f} for our signal, i.e. the matrix diagonal. This additional information changes our state of knowledge about the matrix diagonal in the way that the assumed prior in Eq. (42) is not adequate anymore. However, after only a few samples, \mathbf{f} is not yet a good approximation for the diagonal entries of the matrix, since several entries may be considerably over- or underestimated. By contrast \mathbf{f} provides already a good enough estimator for the trace, see Eq. (61). For that reason one can a priori expect the matrix diagonal $\tilde{\mathbf{s}}$ to be distributed around some $\tilde{\mathbf{t}}$ rather than around zero, where $\tilde{t}_i = \sum_i f_i / r \approx \langle \text{tr}[\mathbf{X}] \rangle_{\{\boldsymbol{\xi}\}} / \dim[\mathbf{X}]$ for all $i \in \{1, \dots, r\}$. Therefore, the prior of the matrix diagonal is chosen to have

a non-zero mean $\tilde{\mathbf{t}}$,

$$P(\tilde{\mathbf{s}}) = \mathcal{G}(\tilde{\mathbf{s}} - \tilde{\mathbf{t}}, \tilde{\mathbf{S}}). \quad (65)$$

As a consequence the filter formulas given by Eq. (50) and (55) undergo a shift,

$$\tilde{\mathbf{m}} = \tilde{\mathbf{D}} \left(\tilde{\mathbf{R}}^\top \tilde{\mathbf{N}}^{-1} \tilde{\mathbf{d}} + \tilde{\mathbf{S}}^{-1} \tilde{\mathbf{t}} \right), \quad (66)$$

$$\tilde{\mathbf{D}} = \left(\tilde{\mathbf{S}}^{-1} + \tilde{\mathbf{R}}^\top \tilde{\mathbf{N}}^{-1} \tilde{\mathbf{R}} \right)^{-1}, \quad (67)$$

$$\tilde{C}_l = \frac{1}{\tilde{\varrho}_l + 2\tilde{\epsilon}_l} \text{tr} \left[\left((\tilde{\mathbf{m}} - \tilde{\mathbf{t}}) (\tilde{\mathbf{m}} - \tilde{\mathbf{t}})^\top + \tilde{\delta}_l \tilde{\mathbf{D}} \right) \tilde{\mathbf{S}}_l^{-1} \right]. \quad (68)$$

Furthermore the noise covariance, i.e. its required inverse, is unknown a priori and needs to be estimated for our algorithm. If the data model described in Sect. 3.3.1. is used, $\tilde{\mathbf{N}}^{-1}$ can be approximated by the noise given the data and an estimator for the signal,

$$\tilde{\mathbf{n}} = \tilde{\mathbf{d}} - \tilde{\mathbf{R}} \tilde{\mathbf{m}}. \quad (69)$$

The calculations are simplified by using,

$$\tilde{\mathbf{N}}^{-1} = \langle \tilde{\mathbf{n}} \tilde{\mathbf{n}}^\top \rangle_{(\tilde{\mathbf{n}})}^{-1} \approx (\text{diag}[\tilde{\mathbf{n}} * \tilde{\mathbf{n}}])^{-1}. \quad (70)$$

This is done in order to limit the computational effort. A more correct treatment of unknown noise covariance matrices is addressed in Oppermann et al. [22].

Eq. (66) to (68) are solved iteratively in the following scheme:

1. Start with $\tilde{\mathbf{m}}^{(\nu=0)} = \mathbf{f}$.
2. Compute $\tilde{\mathbf{n}}^{(\nu+1)}$ according to Eq. (69).
3. Compute $\tilde{C}_l^{(\nu+1)}$ according to Eq. (68), while ignoring $\tilde{\mathbf{t}}$ and $\tilde{\mathbf{D}}$ for $\nu = 0$.
4. Compute $\tilde{\mathbf{m}}^{(\nu+1)}$ according to Eq. (66) using Eq. (67) and (70).
5. Repeat steps 2 to 4 until convergence.

The initial guess for the power spectrum obtained for $\nu = 0$ in step 3 is an overestimate. This accelerates the convergence process as can be seen in the extreme limits: $\tilde{C}_l \rightarrow \infty : \tilde{\mathbf{m}} \sim \tilde{\mathbf{R}}^{-1} \tilde{\mathbf{d}}$, whereas $\tilde{C}_l \rightarrow 0^+ : \tilde{\mathbf{m}} \sim \tilde{\mathbf{t}}$, i.e. a strong overestimate still gives a non trivial result for $\tilde{\mathbf{m}}$, whereas a strong underestimate gives a nearly trivial one.

Following Sect. 2.4.2. the critical filter is to be recommended in general, since it does not exhibit a significant perception threshold. Nevertheless in the considered examples the correction term $\text{tr}[\tilde{\mathbf{D}}\tilde{\mathbf{S}}_l^{-1}]$ contributes only marginally to the accuracy and therefore the classical filter, which does not require the calculation of this term, has been applied in the following.

3.4. Verification & application

3.4.1. Numerical experiments

To verify the proposed algorithm, some numerical experiments that are posed on signals living on the sphere are performed. The examples in this section are represented by all sky HEALPIX¹³ maps with $N_{\text{side}} = 8$, resulting in $r = 768$ pixels and in a maximum spectral index $l_{\text{max}} = 23$ of the spherical harmonics basis in which the signal covariance is assumed to be diagonal due to a statistical isotropy of the signal.¹⁴

Trivial case

At first we consider a trivial case where the matrix in question is given explicitly. To ensure that this matrix is covariant, i.e. it is positive and symmetric, we constructed it to be

$$\mathbf{X} = \begin{pmatrix} X_{11} & -1 & & 0 \\ -1 & \ddots & \ddots & \\ & \ddots & \ddots & -1 \\ 0 & & -1 & X_{rr} \end{pmatrix}, \quad (71)$$

where the diagonal entries need to fulfill $X_{ii} \geq 2 \forall i \in \{1, \dots, r\}$ for positive definiteness and are drawn with a simple structure on the sphere, see Fig. 1.

The normalized L^2 -norms of the residual error¹⁵ serve as an accuracy measure and are shown as a function of CPU time in Fig. 2.

Although this specific operator \mathbf{X} could be implemented very efficiently, the much more expensive full matrix multiplication is used to have realistic computational costs like those of applying a more complex matrix. But this trivial case should only hold as a proof of concept, more sensible examples are discussed in the following.

¹³See HEALPIX homepage <http://healpix.jpl.nasa.gov/>

¹⁴In General a HEALPIX map consists of $12 N_{\text{side}}^2$ pixels and the default maximum spectral index is set to $l_{\text{max}} = 3 N_{\text{side}} - 1$.

¹⁵Meaning mathematically $\|\hat{\mathbf{X}} - \mathbf{f}\|_2/r$ or $\|\hat{\mathbf{X}} - \tilde{\mathbf{m}}\|_2/r$, respectively, to be exact.

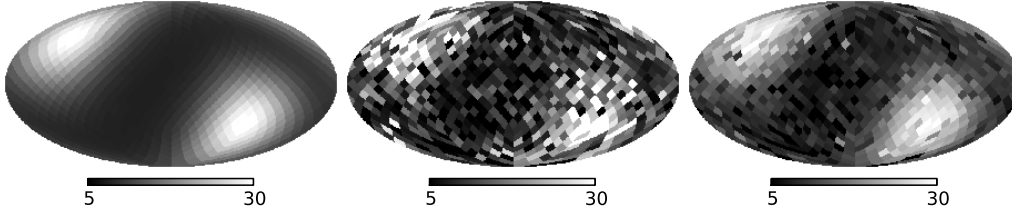


Figure 1: Result from the trivial case: (left) the exact matrix diagonal, (middle) the probing estimate and (right) the Bayesian estimate started with four probes, both after around 0.3 seconds.

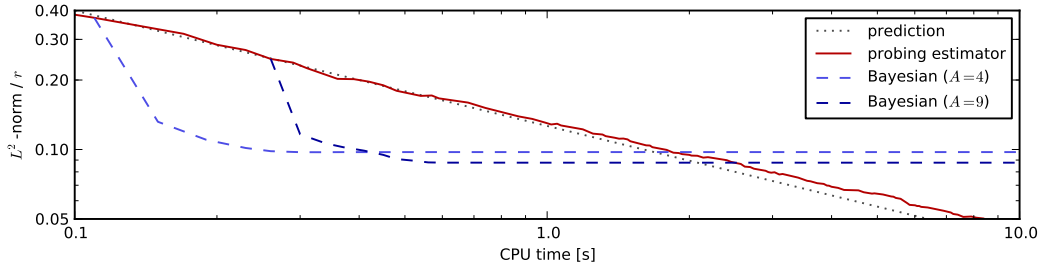


Figure 2: The L^2 -norm of the error (divided by the number of pixels r) as a function of CPU time for the trivial case: The evolution of the probing estimator (solid), its theoretical prediction $\propto 1/\sqrt{A}$ (dotted) and the Bayesian estimators starting with four (dashed light) and nine samples (dashed dark), respectively, are shown.

As one can clearly see in Fig. 2 the probing estimator improves continuously with an increasing number of probes and shows an overall proportionality to $1/\sqrt{A}$ as argued in Sect. 3.2. However, the Bayesian estimator given a set of samples converges in only a couple of iterations to a result whose accuracy the pure probing estimator reaches, at the earliest, after investing a factor of a few more CPU time. For a fixed amount of computation time the Bayesian estimator can excel the probing estimator, as can be seen in Fig. 1. It is also evident that the Bayesian estimator must reach a lower limit in its progress because only a limited data set is provided containing finitely accurate information.

Realistic case

For a more realistic mock example we consider now a covariance matrix $\mathbf{D} = (\mathbf{S}^{-1} + \mathbf{N}^{-1})^{-1}$ similar to the one described in Eq. (50) where the signal covariance \mathbf{S} is completely defined by a power spectrum

$$C_l \propto (\max\{1, l\})^{-2}. \quad (72)$$

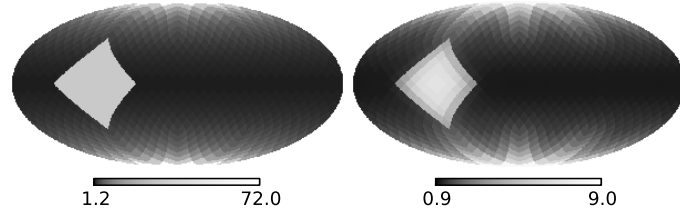


Figure 3: The realistic case: (left) the matrix diagonal of the mock noise covariance \mathbf{N} and (right) the ‘true’ diagonal of the propagator $\mathbf{D} = (\mathbf{S}^{-1} + \mathbf{N}^{-1})^{-1}$.

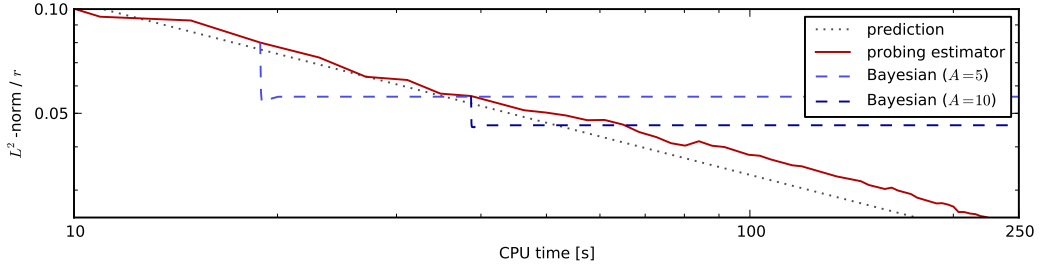


Figure 4: Same as Fig. 2, only for the propagator for the realistic case.

The noise covariance \mathbf{N} is characterized by two effects, first high noise in one of the twelve HEALPIX basis pixels representing a defect in the detector, and second smoothly increased noise towards the poles imitating an observational effect¹⁶. The described noise covariance and the resulting diagonal of the propagator \mathbf{D} are illustrated in Fig. 3, where one can see the conservation of the noise structure and the smoothing effect of the homogeneous signal power spectrum.

The performance of both algorithms is shown in Fig. 4. The inference algorithm performs qualitatively in the same way as in the trivial case but the overall gain in accuracy or time is quantitatively lower. It is also noticeable that the relative advantage of the proposed method decreases with the number of used random vectors. Consequently the matrix diagonal inference method pays off best in cases where a rough estimate using only a few probes is sufficient.

3.4.2. Faraday sky uncertainty

In Oppermann et al. [21] the inference problem of the galactic Faraday depth from the NVSS Rotation Measures Catalogue [32] is addressed. The proposed method has been applied in collaboration with Niels Oppermann to the uncertainty co-

¹⁶The noise variance is assigned to each pixel i according to $N_{ii}^{-1} = (0.005 + 8(h_i(h_i - h_{\max}))^2 / h_{\max}^4)$, where h_i is the HEALPIX ring number associated to the pixel i .

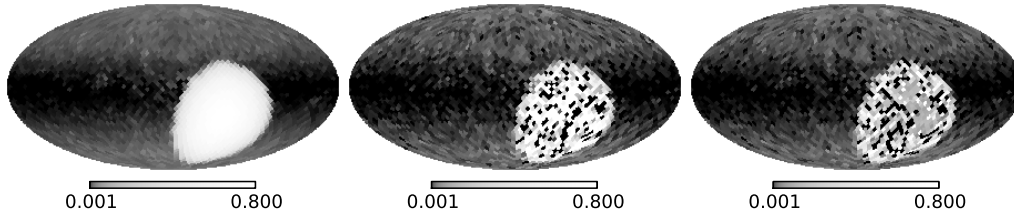


Figure 5: Result from reconstruction of the galactic Faraday depth: (left) the exact matrix diagonal, (middle) the probing estimate after ten iterations and (right) the Bayesian estimate started with ten probes

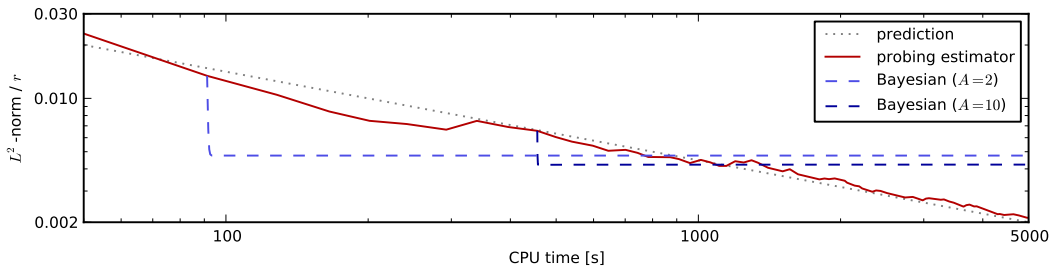


Figure 6: Same as Fig. 2, only for the propagator for the reconstruction of the galactic Faraday depth.

variance matrix of the all sky Faraday depth in order to infer its diagonal. The results, that are briefly shown in Fig. 5 and 6, concur with the previous numerical examples, i.e. the inference method improves also in this case the stochastic estimates, especially the rough ones. A more detailed discussion of this example can be found in Selig et al. [27].

3.5. Conclusions

We reviewed the reliability and robustness of the probing techniques for diagonals of matrices and applied them to several examples where they performed as expected.

A new inference algorithm is described that interprets the probing of the matrix diagonal as a numerical experiment. The outcome of the experiment exhibits all features of a measurement like signal response and noise. Exploiting additional knowledge on the existence of an underlying continuous structure of the matrix diagonal which exhibits a priori unknown correlations allowed for an inference method which improves the estimates acquired from probing.

Applying this new inference algorithm on a sample of matrix probes, estimators for the matrix diagonal are retrieved that exhibit a higher accuracy for a small

investment of additional computation time. As fewer samples are needed by this new method to achieve the same accuracy, the number of computationally expensive calculations is reduced and in this way CPU – and real – time is saved. The new algorithm is especially efficient when matrix diagonals need to be calculated only roughly, since the relative gain in accuracy is larger in cases where only a few probes are available.

This has been shown in numerical examples as well as for the uncertainty map appearing in the reconstruction of the galactic Faraday depth.

4. Photon flux reconstruction & separation

The over three millennia lasting history of astronomy¹⁷ has been broadened from observations of merely visible light to the whole electromagnetic spectrum. The upper frequency domain including both X- and γ -ray¹⁸ is in the focus of high energy astronomy (HEA). An event in this context is defined as the detection of a photon within a given frequency range. Observatories gather also information about the incidence angle of a photon. This spatial information, which of course is subject to uncertainties as all data is, allows for a binning of the photon counts onto a spatial grid. Although some surveys aggregate additional information on the photon's energy, this thesis solely takes photon counts into consideration.

Typical event maps from astrophysical observations exhibit two fundamental, morphological components: On the one hand, there are diffuse structures that spread out smoothly across wide areas of the spatial grid and thus exhibit an intrinsic correlation structure. Such diffuse contributions are often regarded as fore- or background, a distinction that does not matter in this thesis. On the other hand, there are point-like shapes that stem from point sources, bright astrophysical objects with angular extension well below the observational resolution. Their brightness in terms of photon counts may differ from outshining to faint or barely detectable. Both, diffuse and point-like contributions, are superimposed in the data. Ad hoc no photon can be assigned to have been emitted in one kind or the other. Therefore, the inverse problem of signal reconstruction and separation at hand is left for a subsequent analysis.

Previous work

In the last six decades a series of surveys have been performed, from the first X- and γ -ray telescopes on board SAS-A (“Small Astronomy Satellite A”) and Explorer XI to the completed missions of ROSAT (“Röntgensatellit”) and CGRO (“Compton Gamma-Ray Observatory”) to today's active orbital observatories Chandra, XMM-Newton (“X-ray Multi-Mirror”), INTEGRAL (“International Gamma-Ray Astrophysics Laboratory”) and Fermi, to mention a few. In parallel, the development of analysis software for data sets provided by such surveys has advanced with the goal of extracting diffuse structures, e.g. for emission models of the Milky Way or the cosmic X-ray background, or to find new point-like sources, e.g. quasars.

There are many fast and robust but heuristic algorithms that separate those components, e.g. the widely used SExtractor (“Source Extractor”) by Bertin and Arnouts [3] or the CLEAN algorithm by Högbom [16] that has originally been

¹⁷The written history of astronomy reaches back to the earliest Babylonian star catalogs that have been dated from around 1200 BCE.

¹⁸X-ray covers a frequency domain from around 25 PHz to 40 EHz, γ -ray all higher frequencies.

designed for radio astronomy. Also, approaches using wavelet transformation, a technique that goes back to the work of Haar [14, 15], have been carried out with success.

However, algorithms of the Bayesian type are in no way inferior to the heuristic ones. Initially, maximum likelihood methods emerged, as e.g. suggested by Valdes [34] to handle Poisson noise. In the work by Strong [29] an image reconstruction technique based on the ME method is demonstrated analyzing INTEGRAL data. More advanced methods that take full advantage of the Bayesian probability theory ensued. The BSS (“Background-Source Separation”) method described in Guglielmetti et al. [13] treats the background and point-like sources under a two-component mixture model. First, all sources are jointly estimated considering the point-like source contributions as nuisance, and second, the point sources are characterized.

4.1. Problem

The main issue of this section is the reconstruction of the separated diffuse and point-like components from event maps as they can be found in HEA. Although the formalism is stated generally, all applications are restricted to all sky maps. Such spherical maps are provided e.g. by the all sky survey of the X-ray satellite ROSAT or by the Fermi space telescope in the γ -ray domain. The distinctive features of the diffuse and point-like contributions may yield a variety of starting points for heuristic algorithms. An inference algorithm on the other hand may perform superiorly, exploiting additional knowledge, as demonstrated in a different example in the previous Sect. 3. by comparison. The Gibbs free energy formalism is potentially a suitable choice since it allows a Bayesian treatment of the inverse problem, often with a good compromise between being accurate and computationally affordable. A robust reconstruction algorithm should be based on a data model that takes the nature of photon counts and all detector properties into account. The separation of diffuse and point-like signals is then driven by suitable priors. In addition, spectral parameters are incorporated for an appropriate treatment of the a priori unknown diffuse correlation structure.

However, the process of data acquisition poses an especially hard inverse problem because of the nontrivial photon count statistics. It is reasonable to consider the incoming photon flux as being a discrete stream of energy depositions in the detector due to the quantization of light. The number of events fluctuates around some theoretical mean because several random processes are involved in the photon emission, propagation and absorption by the detector. An investigation of those random processes should clarify the importance of these fluctuations and identify the underlying probability distribution that is of significance for the data model.

4.1.1. Poisson distribution & shot noise

In our setting, the detection of a discrete number of photons during a continuous time span is a statistical process. Here, the observation period that may last up to a few megaseconds is still much shorter than any evolutionary time period of an astrophysical object.¹⁹ Therefore, the emission characteristics of sources are assumed to be constant during the observation and the individual events can be regarded as independent and identically distributed random events.

Furthermore, any source emits a huge number of photons. It is reasonable to specify an expected number of photon counts λ for the observation period. The appropriate PDF describing the probability of detecting exactly d photons, if λ are expected, is a Poisson distribution

$$P(d|\lambda) = \mathcal{P}(d; \lambda) = \frac{\lambda^d e^{-\lambda}}{d!}, \quad (73)$$

in the case of statistically independent events. The Poisson distribution has a mean $\langle d \rangle_{\mathcal{P}} = \lambda$ and a variance $\langle d^2 \rangle_{\mathcal{P}}^c = \lambda$. Ergo, the signal-to-noise ratio equals $\sqrt{\lambda}$ and increases as higher photon counts are expected. Nevertheless the Poisson distribution approaches a Gaussian for large numbers and thus exhibits Gaussian noise properties. The influence of the Poissonian noise, also called shot noise, is more severe for low count rates leading to a shrinking signal-to-noise ratio. Therefore, faint objects suffering from shot noise are hard to detect and especially to reconstruct. Fig. 7 illustrates the impact of shot noise onto a typical all sky image from HEA.

4.2. Data model setup

4.2.1. Poisson distributed data

Astronomical X- or γ -ray observations in the high energy regime rely on the detection of single photons. Let the combined field of view of the detector be the whole sky so that the observation can be mapped onto the surface of a sphere. Every real observation is restricted to a finite resolution, i.e. a finite number of detector pixels that usually have equal sizes. Therefore, the observed data vector $\mathbf{d} = (d_1, \dots, d_{N_{\text{pix}}})^{\top}$ naturally consists of the single photon counts that have been measured in each of the N_{pix} pixels.

The expected photon flux varies with respect to different viewing directions because of the different sources on the particular line of sight. As a consequence the photon counts in each pixel vary as well. To take only local, i.e. pixelwise,

¹⁹Varying emission characteristics or spontaneous phenomena, like e.g. γ -ray bursts that typically last several seconds, are not considered which is caveat of this thesis.

noise contributions into account is a common practice that can e.g. be found in [13, 35] and implements the assumption that each photon is recorded in at most one detector element. Thus, the likelihood is formulated as a product of independent Poisson distributions for each pixel $i \in \{1, \dots, N_{\text{pix}}\}$,

$$P(\mathbf{d}|\boldsymbol{\lambda}) = \prod_i \mathcal{P}(d_i; \lambda_i) = \prod_i \frac{\lambda_i^{d_i} e^{-\lambda_i}}{d_i!}, \quad (74)$$

where $\boldsymbol{\lambda}$ contains the expected number of photon counts for each pixel. The expected flux is naturally composed of the flux from all contributing sources and therefore modeled as a sum,

$$\langle \mathbf{d} \rangle_{(\mathbf{d}|\boldsymbol{\lambda})} = \boldsymbol{\lambda} = \boldsymbol{\lambda}_{\mathbf{s}} + \boldsymbol{\lambda}_{\mathbf{u}} + \boldsymbol{\lambda}_{\text{background}} + \dots \quad (75)$$

The two source types of interest are firstly diffuse emission indicated by \mathbf{s} and secondly emission from point-like objects indicated by \mathbf{u} . The related diffuse and point-like signal fields are characterized in Sect. 4.2.3. and 4.2.4., respectively. Any sort of additive background is not taken into consideration in order to keep the model simple. If it is astrophysical, it is regarded to be part of \mathbf{s} .

However, the expectation value $\boldsymbol{\lambda} = \boldsymbol{\lambda}_{\mathbf{s}} + \boldsymbol{\lambda}_{\mathbf{u}}$ expresses photon counts, but the physical photon flux $\boldsymbol{\rho}(\tilde{x})$ as a function of celestial direction \tilde{x} is the quantity to be reconstructed in HEA.²⁰ This photon flux, or source emissivity, determines the expected number of photon counts by an integral over the pixel volume. The expected number of photons can be regarded as the linear response of the measurement system to the signal.

4.2.2. Signal response

The response operator \mathbf{R} describes a linear mapping from the signal phase space onto the data space. In its matrix representation each row i of the response weights the contributions from different parts of the signal that are mapped onto pixel i . As a consequence, a signal coming from a certain position in the sky may contribute to the measurement in several pixels, if not all. Such an entanglement is easily incorporated in the data model by defining the expected counts $\boldsymbol{\lambda}$ to be the detector response to the emissivity $\boldsymbol{\rho}$,

$$\boldsymbol{\lambda} = \mathbf{R} \boldsymbol{\rho}. \quad (76)$$

²⁰Again, a discretization of the coordinate \tilde{x} with r pixels indexed by $x \in \{1, \dots, r\}$ is convenient due to the implementation in a computational environment.

This implementation of the response allows for non-locality in the data model, but conserves the locality of the Poissonian shot noise.

Moreover, the response operator inherits all aspects of the signal detection as argued in Sect. 2.4. It can include a variety of effects due to the survey strategy or the properties of the detector, e.g. an uneven coverage of the survey area on the one hand and the detectors point spread function (PSF) on the other hand. If the response includes a PSF, then the signal is convolved with this PSF and as a result gets smeared out. A delta peak, i.e. an ideal point-like signal, would be spread out to a smooth symmetric blob in the data in case of a Gaussian PSF, i.e. $R_{ix} \equiv \mathcal{G}(x - x_i, \sigma^2)$, where x_i is the center of the PSF of pixel i . Fig. 7 illustrates the convolution of a typical all sky image from HEA with a Gaussian kernel. An adequate description of the detector's functional principle is usually provided by the collaboration responsible for the observation.

In due consideration of the signal response \mathbf{R} , Eq. (75) evolves to

$$\lambda = \mathbf{R}(\boldsymbol{\rho}_s + \boldsymbol{\rho}_u). \quad (77)$$

Although Eq. (77) explains the expected photon counts by means of the photon flux, this physical quantity is an unfavorable signal field for numerical reasons. The emissivity $\boldsymbol{\rho}$ is always non-negative and its values may spread over several orders of magnitude, i.e. $\boldsymbol{\rho}$ varies on logarithmic scales. However, in IFT it is convenient to work with numbers on the full real axis, that are nevertheless well localized. In order to ensure these requirements we reformulate both,

$$\boldsymbol{\rho}_s = \exp(\mathbf{s}) \quad \text{and} \quad \boldsymbol{\rho}_u = \exp(\mathbf{u}), \quad (78)$$

in terms of the diffuse signal field \mathbf{s} and point-like one \mathbf{u} that describe the logarithmic emissivity. The characteristics and a priori assumptions on these signal fields of the inference problem are discussed in the following.

4.2.3. Diffuse signal & spectral parameters

Black-body radiation, bremsstrahlung, synchrotron radiation and inverse Compton scattering, radioactive and pion decay after hadronic interactions, as well as electron-positron annihilation are the main processes leading to radiation in the X- and γ -ray domain. The latest discovery concerning diffuse emission revealed two giant γ -ray bubbles in the Milky Way that are proposed to be a consequence of periodic star capture processes by the central super massive black hole of our own galaxy, see [30, 6]. The diffuse emissivity features smooth patches that span across large areas in the sky. Despite noise, one thus expects to observe similar values in nearby pixels or, in other words, expects the diffuse signal to exhibit strong spatial correlations.

This is modeled by assuming a log-normal distribution for the diffuse emissivity $\rho_{\mathbf{s}} = \exp(\mathbf{s})$, and consequently a normal distribution for the signal field \mathbf{s} ,

$$P(\mathbf{s}) = \mathcal{G}(\mathbf{s}, \mathbf{S}) = \frac{1}{\sqrt{\det[2\pi\mathbf{S}]}} \exp\left(-\frac{1}{2}\mathbf{s}^\top \mathbf{S}^{-1} \mathbf{s}\right), \quad (79)$$

where \mathbf{S} stands again for the signal covariance which encodes the correlation structure.

However, this intrinsic correlation structure is unknown a priori, though statistical isotropy can be assumed because there is no reason to a priori expect different statistics in one viewing direction compared to another.²¹ In Sect. 2.4.2. and App. B, it is discussed how to treat this apparent lack of knowledge. In summary, first, a decomposition of the covariance matrix $\mathbf{S} = \sum_l C_l \mathbf{S}_l$ into spectral coefficients C_l and spectral projection operators \mathbf{S}_l is performed. Second, the parameters C_l are included in the formalism, where the lack of spectral knowledge is expressed by the setup of spectral priors $P(C_l)$ that are flat on a logarithmic scale.

4.2.4. Point-like signal

Point-like signals summarize the peaking flux from all point sources. The set of point source classes in the high energy regime involves a long list of objects, the most eminent ones are the distant active galactic nuclei. According to the cosmological principle such sources follow a statistically isotropic distribution on the sky. Furthermore, point sources on the sky are assumed here to be independent of each other. We assume the same for the point-like signals of the individual pixels. Note that, two sources being close to each other on the observational sphere may nevertheless have huge physical distances in the radial direction.

Under the assumption of a Euclidean universe with a homogeneous distribution of point sources, the number of source counts $N \propto L^3$ scales with the distance cubed. The spherical emission of each source in turn causes the observable brightness $S \propto L^{-2}$ to depend on the surface of the propagation sphere. As a consequence, the number of point sources $N \propto S^{-1.5}$ is proportional to the brightness to the power of -1.5 [11].²² Although this $\log S / \log N$ relation is based on crude geometric assumptions, it agrees surprisingly well with observations, see e.g. [33].

Therefore, the point source brightness distribution should follow a power law. But a power law prior cannot be normalized and would allow for an infinite number of infinitesimally faint point sources, which is unphysical. With a cutoff at the

²¹Anisotropies introduced by the presence of a galactic disk can be dealt with by an appropriate redefinition of the diffuse signal, cf. [21].

²²In order to avoid Olbers' paradox, physical aspects, as e.g. the redshift-distance relation, need to be included.

lower end, the power law may become an inverse-gamma distribution which has been introduced in Sect. 2.4.2. Thus, independent priors for the emissivity $\rho_{\mathbf{u}}$ in each pixel are assumed,

$$P(\rho_{\mathbf{u}}) = \mathcal{I}(\rho_{\mathbf{u}}; \eta, \zeta) = \frac{1}{\zeta \Gamma(\eta - 1)} \left(\frac{\rho_{\mathbf{u}}}{\zeta} \right)^{-\eta} \exp \left(-\frac{\zeta}{\rho_{\mathbf{u}}} \right), \quad (80)$$

where η is the shape and ζ the scale parameter. Following the previous argumentation, the shape parameter is set to the fixed value of $\eta = 1.5$. In the mock examples the scale parameter is also fixed to $\zeta = 1.0$. In principle the IFT formalism would allow for a priori unknown parameters but this extension is left open for future research.

The prior for the point-like signal \mathbf{u} is retrieved from Eq. (80) with due regard to the Jacobian,

$$\begin{aligned} P(\mathbf{u}) &= \prod_x \mathcal{I}(\exp(u_x); \eta, \zeta) \left| \frac{d(\rho_{\mathbf{u}})_x}{du_x} \right| \\ &= \prod_x \frac{1}{\Gamma(\eta - 1)} \left(\frac{\exp(u_x)}{\zeta} \right)^{-(\eta-1)} \exp \left(-\frac{\zeta}{\exp(u_x)} \right). \end{aligned} \quad (81)$$

In order to keep the notation simple, the parameters η and ζ are promoted in Sect. 4.3. to vectors with all components being equal, i.e. $\boldsymbol{\eta} = \eta \mathbf{1}$ and $\boldsymbol{\zeta} = \zeta \mathbf{1}$.

4.2.5. Data model summary

Before applying the minimum Gibbs free energy formalism in Sect. 4.3. let us summarize the relevant parts of the complete data model:

- The likelihood is a Poisson distribution assuming independent local shot noise, $P(\mathbf{d}|\mathbf{s}, \mathbf{u}, C) = \mathcal{P}(\mathbf{d}; \boldsymbol{\lambda})$ with $\boldsymbol{\lambda} = \mathbf{R}(\exp(\mathbf{s}) + \exp(\mathbf{u}))$.
- The prior for the diffuse component is a normal distribution, $P(\mathbf{s}|C) = \mathcal{G}(\mathbf{s}, \mathbf{S})$, for a given power spectrum of \mathbf{S} .
- The prior for the unknown power spectrum of $\mathbf{S} = \sum_l C_l \mathbf{S}_l$ is given by independent priors for each spectral parameter C_l , $P(C) = \prod_l P(C_l)$.
- The prior for each spectral parameter C_l is modeled to be flat on a logarithmic scale, $P(C_l) = \mathcal{I}(C_l; \alpha_l, q_l)$ with $\alpha_l \rightarrow 1^+$ and $q_l \rightarrow 0^+$.
- The prior $P(\mathbf{u})$ for the point-like component is derived from independent inverse-gamma distributions with known shape $\eta = 1.5$ and scale parameter $\zeta = 1.0$.

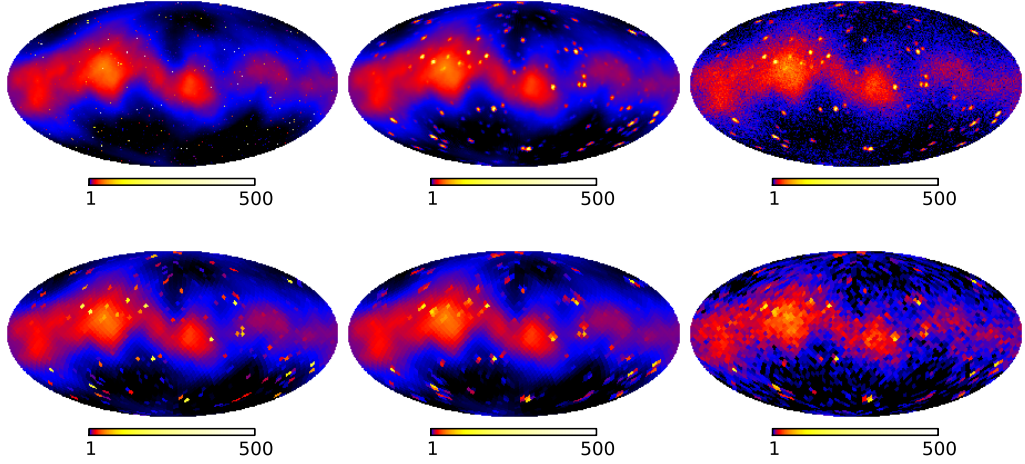


Figure 7: Data generation chain presented in event maps with logarithmic scales: (top) with a resolution equivalent to HEALPIX parameter $N_{\text{side}} = 64$ and (bottom) $N_{\text{side}} = 16$; (left) the unconvolved expected photon counts from the original signals, (middle) the expected photon counts including a Gaussian convolution with a 1° standard deviation on the sphere, and (right) the resulting data including local shot noise.

This data model provides an approximation of the signal characteristics and describes the process of data generation from these signals. Hence, a posterior PDF is modeled to explain a given data set in terms of the diffuse and point-like signals as well as the spectral parameters.

Furthermore, the data model allows for the generation of mock signals and their processing to mock data. The advantage of analyzing mock data is obviously the existing knowledge on the original signals that allows for a subsequent comparison to the reconstruction. Two such data generation chains are illustrated in Fig. 7.

4.3. Gibbs free energy of the combined photon flux

4.3.1. Derivation

The minimum Gibbs free energy formalism [10] that has been outlined in Sect. 2.3. is chosen to solve the problem of photon flux reconstruction and separation. Let us briefly recapitulate that the Gibbs free energy describes the information theoretical distance between the original posterior PDF and its approximation, and that its minimization provides an estimator for the map by means of the posterior mean field and the corresponding uncertainty information on this map.

Following Eq. (32) the approximation of the posterior $P(\mathbf{s}, \mathbf{u}|\mathbf{d})$ is chosen to

be a Gaussian distribution,

$$P(\mathbf{s}, \mathbf{u}|\mathbf{d}) \approx P(\mathbf{s}, \mathbf{u}|\mathbf{m}, \mathbf{D}) = P(\boldsymbol{\phi}|\mathbf{D}) = \mathcal{G}(\boldsymbol{\phi}, \mathbf{D}), \quad (82)$$

with an argument $\boldsymbol{\phi}$ and an uncertainty covariance matrix \mathbf{D} . These quantities are defined in the combined phase space of the signals \mathbf{s} and \mathbf{u} that are subject to the inference,

$$\boldsymbol{\phi} = \begin{pmatrix} \mathbf{s} \\ \mathbf{u} \end{pmatrix} - \underbrace{\begin{pmatrix} \mathbf{m}_s \\ \mathbf{m}_u \end{pmatrix}}_{\mathbf{m}} \quad \text{and} \quad \mathbf{D} = \begin{pmatrix} \mathbf{D}_s & \mathbf{D}_{su} \\ \mathbf{D}_{su}^\top & \mathbf{D}_u \end{pmatrix}, \quad (83)$$

where \mathbf{m} is the map that minimizes the Gibbs free energy together with the uncertainty covariance matrix \mathbf{D} . Consequently, the minimizing maps \mathbf{m}_s and \mathbf{m}_u describe the most reasonable field configuration of the separated signal reconstruction within the assumed Gaussian approximation.

The next step is to retrieve the information Hamiltonian implied by the data model using the product rule, cf. Eq. (6),

$$\begin{aligned} H(\mathbf{s}, \mathbf{u}, C) &= -\log P(\mathbf{d}, \mathbf{s}, \mathbf{u}, C) \\ &= -\log P(\mathbf{d}|\mathbf{s}, \mathbf{u}, C) - \log (P(\mathbf{s}|C)P(C)) - \log P(\mathbf{u}). \end{aligned} \quad (84)$$

Plugging in the contributions from the likelihood, the diffuse and the point-like signal prior, see Eq. (74), (79) and (81), the Hamiltonian reads,

$$\begin{aligned} H(\mathbf{s}, \mathbf{u}, C) &= H_0 + \mathbf{1}^\top \boldsymbol{\lambda} - \mathbf{d}^\top \log \boldsymbol{\lambda} \\ &\quad + \frac{1}{2} \mathbf{s}^\top \mathbf{S}^{-1} \mathbf{s} + \frac{1}{2} \log |2\pi \mathbf{S}| + \sum_l \left(\alpha_l \log C_l + \frac{q_l}{C_l} \right) \\ &\quad + (\boldsymbol{\eta} - \mathbf{1})^\top \mathbf{u} + \boldsymbol{\zeta}^\top \exp(-\mathbf{u}), \end{aligned} \quad (85)$$

where the expected number of counts $\boldsymbol{\lambda}$ equals $\mathbf{R}(\exp(\mathbf{s}) + \exp(\mathbf{u}))$. All constant terms are absorbed into

$$H_0 = \mathbf{1}^\top \log \mathbf{d}! - \sum_l \log \left(\frac{q_l^{(\alpha_l-1)}}{\Gamma(\alpha_l-1)} \right) - \int dx \log \left(\frac{\zeta^{(\eta-1)}}{\Gamma(\eta-1)} \right).$$

However, the Hamiltonian given by Eq. (85) still exhibits an explicit dependence on the spectral parameters C_l . Those are considered to be nuisance parameters since the power spectrum is not the primary goal of our inference. In order to get

rid of this dependence the Hamiltonian is marginalized as follows,

$$H(\mathbf{s}, \mathbf{u}) = -\log \left(\left(\prod_l \int dC_l \right) \exp(-H(\mathbf{s}, \mathbf{u}, C)) \right) \quad (86)$$

$$\begin{aligned} &= H'_0 + \mathbf{1}^\top \boldsymbol{\lambda} - \mathbf{d}^\top \log \boldsymbol{\lambda} \\ &\quad + \sum_l \gamma_l \log \left(q_l + \frac{1}{2} \mathbf{s}^\top \mathbf{S}_l^{-1} \mathbf{s} \right) \\ &\quad + (\boldsymbol{\eta} - \mathbf{1})^\top \mathbf{u} + \boldsymbol{\zeta}^\top \exp(-\mathbf{u}), \end{aligned} \quad (87)$$

$$H'_0 = H_0 + \sum_l \log \left(\frac{1}{\Gamma(\gamma_l)} \sqrt{\det[2\pi \tilde{\mathbf{S}}_l]} \right),$$

where $\gamma_l = \alpha_l - 1 + \varrho_l/2$ and ϱ_l stands again for the degrees of freedom for each spectral band. A complete lack of knowledge of the power spectrum can be described by the limit of $\alpha_l \rightarrow 1^+$ and $q_l \rightarrow 0^+$ corresponding to a logarithmically flat prior.

Next, the internal energy needs to be determined. This is done by calculating the expectation value of the Hamiltonian weighted by the posterior ansatz $\mathcal{G}(\boldsymbol{\phi}, \mathbf{D})$,

$$U = \langle H(\mathbf{s}, \mathbf{u}) \rangle_{(\mathbf{s}, \mathbf{u}|\mathbf{d})} \approx \langle H(\mathbf{s}, \mathbf{u}) \rangle_{(\boldsymbol{\phi}|\mathbf{D})} = \tilde{U}(\mathbf{m}, \mathbf{D}). \quad (88)$$

However, the expectation value cannot be calculated in closed-form. Therefore, each term is dealt with separately.

The first contribution from the likelihood can be treated analytically,

$$\langle \mathbf{1}^\top \boldsymbol{\lambda} \rangle_{(\boldsymbol{\phi}|\mathbf{D})} = \mathbf{1}^\top \boldsymbol{\mu}, \quad (89)$$

$$\boldsymbol{\mu} = \mathbf{R} \left(\exp \left(\mathbf{m}_s + \frac{1}{2} \hat{\mathbf{D}}_s \right) + \exp \left(\mathbf{m}_u + \frac{1}{2} \hat{\mathbf{D}}_u \right) \right), \quad (90)$$

where the quantity $\boldsymbol{\mu} = \langle \boldsymbol{\lambda} \rangle_{(\boldsymbol{\phi}|\mathbf{D})} \approx \langle \mathbf{d} \rangle_{(\mathbf{d}|\mathbf{m}, \mathbf{D})}$ is introduced, which expresses the expectation value of the data given the map and the uncertainty covariance matrices of \mathbf{s} and \mathbf{u} . In other words, $\boldsymbol{\mu}$ describes the expected data that would result from the reconstruction, i.e. the reconstructed signals and the according uncertainties. Therefore, $\boldsymbol{\mu}$ imitates the observed data, up to restrictions by the priors, in order to satisfy the likelihood.

The next terms include logarithmic expressions in Gaussian integrals and thus evade analytic solutions. The expansion of the logarithm as an asymptotic power series around the expectation value of its argument provides a way out. With the definition of $\boldsymbol{\mu} = \langle \boldsymbol{\lambda} \rangle_{(\boldsymbol{\phi}|\mathbf{D})}$ in mind, this reads for the second non-constant term in

Eq. (87),

$$\langle -\mathbf{d}^\top \log \boldsymbol{\lambda} \rangle_{(\phi|\mathbf{D})} = -\mathbf{d}^\top \log \boldsymbol{\mu} - \mathbf{d}^\top \left\langle \log \frac{\boldsymbol{\lambda}}{\boldsymbol{\mu}} \right\rangle_{(\phi|\mathbf{D})} \quad (91)$$

$$\simeq -\mathbf{d}^\top \log \boldsymbol{\mu} + \mathbf{d}^\top \sum_{\nu=2}^{\infty} \frac{(-1)^\nu}{\nu} \underbrace{\left\langle \left(\frac{\boldsymbol{\lambda}}{\boldsymbol{\mu}} - \mathbf{1} \right)^\nu \right\rangle_{(\phi|\mathbf{D})}}_{[\mathbf{I}]^{(\nu)}}. \quad (92)$$

The same procedure is applied to the contributions from the diffuse signal prior,

$$\begin{aligned} \langle \gamma_l \log (q_l + \tfrac{1}{2} \mathbf{s}^\top \mathbf{S}_l^{-1} \mathbf{s}) \rangle_{(\phi|\mathbf{D})} &\simeq \gamma_l \log (q_l + \tfrac{1}{2} \text{tr} [\mathbf{B}_l]) \\ &\quad - \gamma_l \sum_{\nu=2}^{\infty} \frac{(-1)^\nu}{\nu} \underbrace{\left\langle \left(\frac{q_l + \tfrac{1}{2} \mathbf{s}^\top \mathbf{S}_l^{-1} \mathbf{s}}{q_l + \tfrac{1}{2} \text{tr} [\mathbf{B}_l]} - \mathbf{1} \right)^\nu \right\rangle_{(\phi|\mathbf{D})}}_{[\mathbf{II}]_l^{(\nu)}}, \end{aligned} \quad (93)$$

where $\mathbf{B}_l = (\mathbf{m}_s \mathbf{m}_s^\top + \mathbf{D}_s) \mathbf{S}_l^{-1}$. It is computationally not feasible to implement all terms involving $[\mathbf{I}]^{(\nu)}$ or $[\mathbf{II}]_l^{(\nu)}$, respectively. Ergo, the expansion is truncated at some order ν_{\max} and all accounted corrections are summarized as

$$\Delta^{(\nu_{\max})} = \mathbf{d}^\top \sum_{\nu=2}^{\nu_{\max}} \frac{(-1)^\nu}{\nu} [\mathbf{I}]^{(\nu)} - \sum_l \gamma_l \sum_{\nu=2}^{\nu_{\max}} \frac{(-1)^\nu}{\nu} [\mathbf{II}]_l^{(\nu)}. \quad (94)$$

The second order corrections $\Delta^{(2)}$ are detailed in App. C. In the following we only consider the zeroth order²³ whose implementation is computationally manageable.

The last term that completes the expression for the internal energy stems from the diffuse signal prior and can be calculated in closed-form,

$$\langle (\boldsymbol{\eta} - \mathbf{1})^\top \mathbf{u} + \boldsymbol{\zeta}^\top \exp(-\mathbf{u}) \rangle_{(\phi|\mathbf{D})} = (\boldsymbol{\eta} - \mathbf{1})^\top \mathbf{m}_u + \boldsymbol{\zeta}^\top \exp \left(-\mathbf{m}_u + \tfrac{1}{2} \hat{\mathbf{D}}_u \right). \quad (95)$$

The entropy for the Gaussian posterior ansatz is already given by Eq. (34). Thus,

²³The first order of the expansion of the logarithm vanishes, i.e. $[\mathbf{I}]^{(1)} = 0$ and $[\mathbf{II}]_l^{(1)} = 0$.

the Gibbs free energy reads according to Eq. (39),

$$\begin{aligned}
 G(\mathbf{m}, \mathbf{D}) &= \tilde{U}(\mathbf{m}, \mathbf{D}) - T\tilde{S}_B(\mathbf{D}) \\
 &= G_0 + \mathbf{1}^\top \boldsymbol{\mu} - \mathbf{d}^\top \log \boldsymbol{\mu} \\
 &\quad + \sum_l \gamma_l \log \left(q_l + \frac{1}{2} \text{tr} [(\mathbf{m}_s \mathbf{m}_s^\top + \mathbf{D}_s) \mathbf{S}_l^{-1}] \right) \\
 &\quad + (\boldsymbol{\eta} - \mathbf{1})^\top \mathbf{m}_u + \boldsymbol{\zeta}^\top \exp \left(-\mathbf{m}_u + \frac{1}{2} \hat{\mathbf{D}}_u \right) \\
 &\quad - \frac{T}{2} \log (\det [\mathbf{D}]), \\
 G_0 &= H'_0 - \frac{T}{2} (1 + \log(2\pi)) \text{tr}[\mathbf{1}],
 \end{aligned} \tag{96}$$

where still $\boldsymbol{\mu} = \mathbf{R}(\exp(\mathbf{m}_s + \frac{1}{2} \hat{\mathbf{D}}_s) + \exp(\mathbf{m}_u + \frac{1}{2} \hat{\mathbf{D}}_u))$. The number of degrees of freedom that the Gibbs free energy exhibits is of the order $\mathcal{O}(N_{\text{pix}}^2)$. However, a minimization does not yield an explicit solution of the inverse problem in closed-form. We investigate the character of the solution and a possible ansatz in the following.

4.3.2. Self-consistent solution

Of primary interest are the maps \mathbf{m}_s and \mathbf{m}_u for which the derivatives of the Gibbs free energy given by Eq. (96) yield,

$$\frac{\delta G}{\delta \mathbf{m}_s} = \mathbf{r} * e^{\mathbf{m}_s + \frac{1}{2} \hat{\mathbf{D}}_s} + \mathbf{S}^{-1} \mathbf{m}_s, \tag{97}$$

$$\frac{\delta G}{\delta \mathbf{m}_u} = \mathbf{r} * e^{\mathbf{m}_u + \frac{1}{2} \hat{\mathbf{D}}_u} + (\boldsymbol{\eta} - \mathbf{1}) - \boldsymbol{\zeta} * e^{-\mathbf{m}_u + \frac{1}{2} \hat{\mathbf{D}}_u}. \tag{98}$$

The quantity $\mathbf{r} = \mathbf{R}^\top (\mathbf{1} - \mathbf{d}/\boldsymbol{\mu})$ describes the response weighted relative discrepancy between the data \mathbf{d} and the reconstructed data expectation $\boldsymbol{\mu}$. This term is negative when the number of photon counts is larger than predicted by the model, and positive in the opposite case. Second, the inverse diffuse signal covariance \mathbf{S}^{-1} replaces the parameter sum $\sum_l C_l^{-1} \mathbf{S}_l^{-1}$ in Eq. (97) due to the reidentification of the spectral parameters

$$C_l = \frac{1}{\gamma_l} \left(q_l + \frac{1}{2} \text{tr} [(\mathbf{m}_s \mathbf{m}_s^\top + \mathbf{D}_s) \mathbf{S}_l^{-1}] \right). \tag{99}$$

This result is expected since the same was found for the critical filter [8], see Sect. 2.4.2.

Furthermore, the derivation of the Gibbs free energy with respect to the uncertainty matrix \mathbf{D} yields another insight on the solution. First, consider the off-diagonal block \mathbf{D}_{su} and its determining equation,

$$\frac{\delta G}{\delta \mathbf{D}_{su}} = \mathbb{0} = -T (\mathbf{D}_s^{-1} \mathbf{D}_{su} \mathbf{D}_u^{-1}), \quad (100)$$

where $\mathbb{0}$ stands for a zero matrix. Since \mathbf{D}_s and \mathbf{D}_u are covariance matrices themselves, i.e. they are strictly positive and more importantly their inverses exist, all entries of \mathbf{D}_{su} vanish according to Eq. (100) in the minimum of the Gibbs free energy within the made approximations. Therefore, we assume $\mathbf{D}_{su} = \mathbb{0}$ in the following. The derivatives of the Gibbs free energy with respect to \mathbf{D}_s and \mathbf{D}_u then read

$$\frac{\delta G}{\delta \mathbf{D}_s} = \mathbb{0} = \frac{1}{2} \text{diag} [\mathbf{r} * e^{\mathbf{m}_s + \frac{1}{2} \hat{\mathbf{D}}_s}] + \frac{1}{2} \mathbf{S}^{-1} - \frac{T}{2} \mathbf{D}_s^{-1}, \quad (101)$$

$$\frac{\delta G}{\delta \mathbf{D}_u} = \mathbb{0} = \frac{1}{2} \text{diag} [\mathbf{r} * e^{\mathbf{m}_u + \frac{1}{2} \hat{\mathbf{D}}_u}] + \frac{1}{2} \text{diag} [\boldsymbol{\zeta} * e^{-\mathbf{m}_u + \frac{1}{2} \hat{\mathbf{D}}_u}] - \frac{T}{2} \mathbf{D}_u^{-1}. \quad (102)$$

Those equations can be solved for the covariances, leading to

$$\mathbf{D}_s = T \left(\text{diag} [\mathbf{r} * e^{\mathbf{m}_s + \frac{1}{2} \hat{\mathbf{D}}_s}] + \mathbf{S}^{-1} \right)^{-1}, \quad (103)$$

$$\mathbf{D}_u = T \left(\text{diag} [\mathbf{r} * e^{\mathbf{m}_u + \frac{1}{2} \hat{\mathbf{D}}_u} + \boldsymbol{\zeta} * e^{-\mathbf{m}_u + \frac{1}{2} \hat{\mathbf{D}}_u}] \right)^{-1}. \quad (104)$$

The structure of these matrices is similar to the one known for the Wiener filter, cf. Eq. (50), where we calculated

$$\mathbf{D} = T (\mathbf{M} + \mathbf{S}^{-1})^{-1}. \quad (105)$$

Thus, we can understand the individual terms that contribute to the propagators in Eq. (103) and (104) by analogy to Eq. (105). First, the likelihood uncertainties that correspond to $\mathbf{M} = \mathbf{R}^T \mathbf{N}^{-1} \mathbf{R}$ are expressed by the terms $\text{diag}[\mathbf{r} * \exp(\dots)]$. Second, the prior covariance matrices are identified to be \mathbf{S}^{-1} and $\text{diag}[\boldsymbol{\zeta} * \exp(\dots)]$, respectively. Note that the complete covariance matrix \mathbf{D}_u of the point-like signal is diagonal in the pixel basis. This is sensible due to the assumed independence of point-like sources.

Moreover, Eq. (103) and (104) provide a solution for \mathbf{D}_s and \mathbf{D}_u and their inverses that depends only on the mean fields, the diagonals of their uncertainty matrices, and the power spectrum. Those equations allow the implementation of the covariance matrices \mathbf{D}_s and \mathbf{D}_u in form of a computer routine instead of an explicit treatment. Thereby, the remaining degrees of freedom are reduced from

the order of $\mathcal{O}(N_{\text{pix}}^2)$ down to $\mathcal{O}(N_{\text{pix}})$.

4.3.3. Gradient approach

The Gibbs free energy is a scalar quantity in a very high dimensional space. In addition, strong correlations exist between many of the degrees of freedom. This prohibits the convergence of purely iterative solvers. However, a semi-iterative solver, i.e. an alternating evaluation of the power spectrum on the one hand and all other degrees of freedom on the other hand, is conceivable. Further, a good solver should be adapted to the characteristics of the problem. For the purpose of gaining an impression of the shape of the energy landscape over this high dimensional space one can exemplarily reduce the degrees of freedom down to a presentable number, say two, i.e. the whole measurement regards only one single pixel. Fig. 8 illustrates the Gibbs free energy in dependence of the one-dimensional maps m_s and m_u assuming known uncertainties.

A potentially suitable strategy for finding the minimum of the Gibbs free energy is a gradient approach. The underlying postulate is that the Gibbs free energy is smooth and exhibits only one minimum. This postulate is insofar justified as the posterior ansatz is a multi-dimensional Gaussian distribution which describes a quadratic potential with exactly one minimum. The idea behind such a gradient approach is to follow the descent, i.e. the negative gradient, step-by-step downhill towards the minimum until a tolerance area around the minimum has been reached.

In order to make the algorithm computationally feasible the Gibbs free energy is minimized with respect to a combined field that represents only the essential degrees of freedom. This combined field $(\mathbf{m}_s^\top, \mathbf{m}_u^\top, \hat{\mathbf{D}}_s^\top, \hat{\mathbf{D}}_u^\top)^\top$ consists of the signal maps and the diagonals of the covariances. The latter are sufficient because the full covariance matrix is given by the combined fields, cf. Eq. (103) and (104). It remains firstly to choose a starting point for the gradient approach, and secondly to clarify how the intermediate step sizes are to be chosen.

Suitable starting values that are close to the minimum can easily be obtained by a simple heuristic pre-analysis of the data. First, one computes a smoothed version of the data and its overall variance σ^2 . Second, the data is compared to this smoothed version and all pixels in which the difference exceeds a 3σ -threshold are classified to host a point-like source. Here, the choice of 3σ as the threshold is arbitrary but typical for detection thresholds. The resulting source map yields a point-like starting signal and the cleaned and smoothed data a diffuse starting signal. Third, the uncertainties are guessed by the squared differences to the data.

However, the choice of the step size is delicate, since a too small step size in case of a flat descent wastes computational effort and a too big step size in case of a steep descent could lead to divergence. The best choice would be an adaptive step size that is computationally cheap. Furthermore, a convenient step-

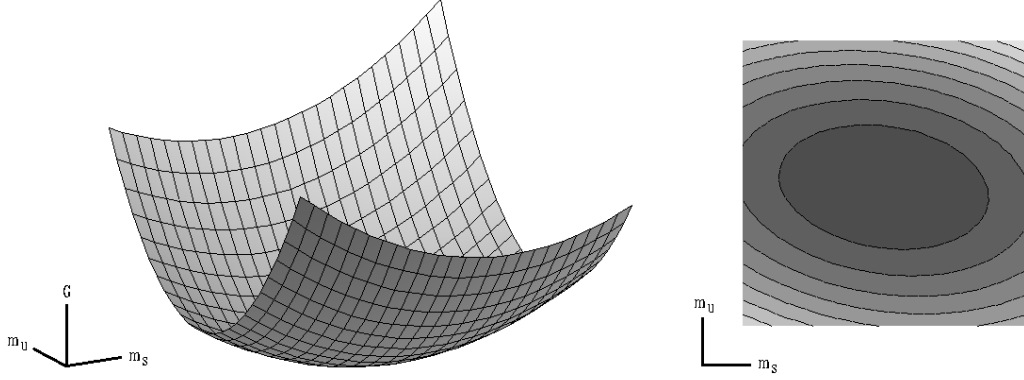


Figure 8: Sketch of the Gibbs free energy G landscape with an exemplary reduction of the degrees of freedom down to two, m_u and m_s , regarding only one single pixel: (left) a 3D plot and (right) the according contour plot.

by-step convergence against the minimum should exhibit smooth variations in the combined field. The angle between the current gradient and the one at the next position expresses the overall change in the combined field. If all entries in the gradient change signs the angle equals π and the algorithm steps back in the opposite direction, whereas an infinitesimal change brings the angle close to zero and the algorithm steps straight on in the same direction. Therefore, a selection criterion for the step size is defined on the basis of the angle between step directions and given the previous step size as listed in Tab. 2. This simple implementation is functional and in practice the considered angle is at maximum rejected twice.

Hence, all required parts of a gradient approach, i.e. analytic expressions for the gradient, the full covariance matrices, and the power spectrum, as well as a step-by-step algorithm, are clarified. This approach provides the following scheme for the minimization of the Gibbs free energy:

1. Set initials for the combined field, i.e. for m_s , \hat{D}_s , m_u , \hat{D}_u and C_l .
2. Compute all related quantities, i.e.
 Update the diagonals of D_s^{-1} and D_u^{-1} according to Eq. (103) and (104),
 Compute the spectral coefficients C_l according to Eq. (99).
3. Compute the combined gradient according to Eq. (97), (98), (101) and (102)
4. Compute the step size according to Tab. 2 and the resulting new combined field.
5. Repeat steps 2 to 4 until convergence.

consideration	action
$\alpha < \pi/4$	set $o_{\text{new}} = 2 \cdot o_{\text{old}}$
$\pi/4 \leq \alpha < \pi/2$	set $o_{\text{new}} = o_{\text{old}}$
$\pi/2 \leq \alpha$	reject; test for $o_{\text{old}}/3$

Table 2: Selection criteria for the step size o_{new} of the gradient approach based on the angle $\alpha(o_{\text{old}})$ between the current gradient and the one at the next position, and given the previous step size o_{old} .

The computationally most expensive step is the second, where matrix diagonals need to be updated. This is usually done by probing techniques but the procedure presented in Sect. 3. may provide remedy. Especially here, where the diagonals from the previous iteration cycle are available and their changes are small due to the step algorithm, rough estimates based on only a few sampling probes are sufficient.

4.4. Application results

4.4.1. Tempering

Two mock problems of separating diffuse and point-like sources are investigated without the complication of instrumental point spread functions. These are posed on the sphere and used to verify the developed algorithm. All maps shown in this section are represented by HEALPIX maps with $N_{\text{side}} = 8$, resulting in $N_{\text{pix}} = 768$ pixels and in a maximum spectral index $l_{\text{max}} = 23$. Ergo the number of degrees of freedom is already of the order $\mathcal{O}(10^3)$, although the resolution is rather low.

The remaining parameter that needs to be fixed before putting the algorithm to work is the temperature T . As argued in Sect. 2.3., where the thermodynamical inference has been detailed, the temperature specifies whether the MAP or ME method is to be preferred, and $T = 1$ corresponds to a compromise that preserves the untempered posterior. Since the reconstructed signal fields are entangled and because of their exponential responses, the Gibbs free energy is expected to exhibit steep descents. Therefore, a lower temperature that narrows the tempered posterior in favor of the MAP solution seems worth considering. The problem of signal reconstruction and separation given the data has been solved for two low temperatures, i.e. $T = 0.05$ and $T = 0.5$ to be exact. In Fig. 9, 10 and 11 the resulting power spectra, and all sky maps of the original signals and their reconstructions, as well as the pixelwise relative standard deviations are shown.

A coarse visual inspection of the original and the reconstructed signals in Fig. 10 and 11 reveals a good agreement, i.e. that both essential data processing steps, the signal reconstruction and separation, have been conducted successfully. Note

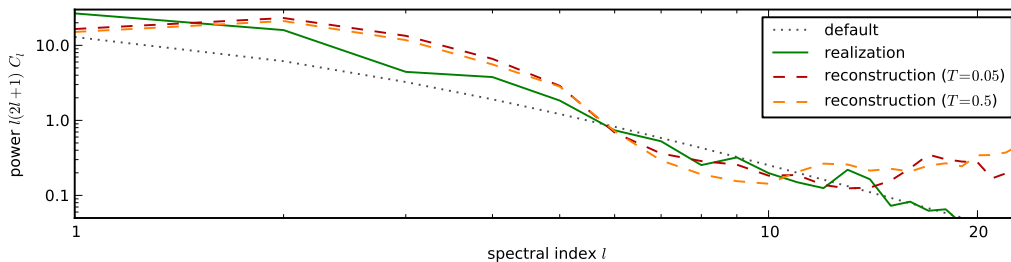


Figure 9: Diffuse signal power spectra: (solid) the power spectrum realization of the original diffuse signal drawn from a (dotted) default one, (dashed dark) the reconstructed spectra for $T = 0.05$ and (dashed light) for $T = 0.5$.

that the uncertainty is given pixelwise and in its relative value for the purpose of an unbiased presentation with respect to the absolute number of photon counts. Further, the standard deviation is to be interpreted by means of a log-normal distribution because of the Gaussian posterior ansatz for the signal reconstruction, i.e. the intuitive interpretation by means of Gaussian uncertainties is only applicable on logarithmic scales.

A more detailed inspection of the results seems in order. The reconstruction of the diffuse maps is pixelated and exhibits a slight checkerboard pattern. The reason for this is an inaccurate reconstruction on small scales that becomes obvious when looking at the power spectrum reconstruction in Fig. 9. The large and intermediate scale power is adequately reconstructed resulting in the evident agreement of original and reconstructed maps on these scales. Nonetheless, the power on small scales is overestimated. This overestimation is slightly more distinct in the case of $T = 0.5$ than it is for $T = 0.05$. This fault is caused by the numerous use of the HEALPIX-internal basis transformations that, despite all their advantages in speed and computational convenience, are known to exhibit numerical flaws regarding results in the upper third of the spectrum. As a consequence the reconstructed spectrum on small scales, i.e. at large l , is overestimated and the filter is less discriminative against noise on those scales, cf. Eq. (99). In addition, the small-scale uncertainties get also overestimated, leading to relatively large uncertainties for the individual pixels. The power spectrum reconstruction provides a better impression of the reconstruction reliability than those pixel uncertainty maps since it illustrates the uncertainties for the individual scales, not the individual pixels.

Furthermore, the detection of point-like sources features two aspects. On the one hand, the reconstruction accuracy is obviously limited by the coarse Poisson statistics of the data. Faint sources that have not been detected, i.e. those which did not imprint sufficiently on the data to stick out of the shot noise of the diffuse

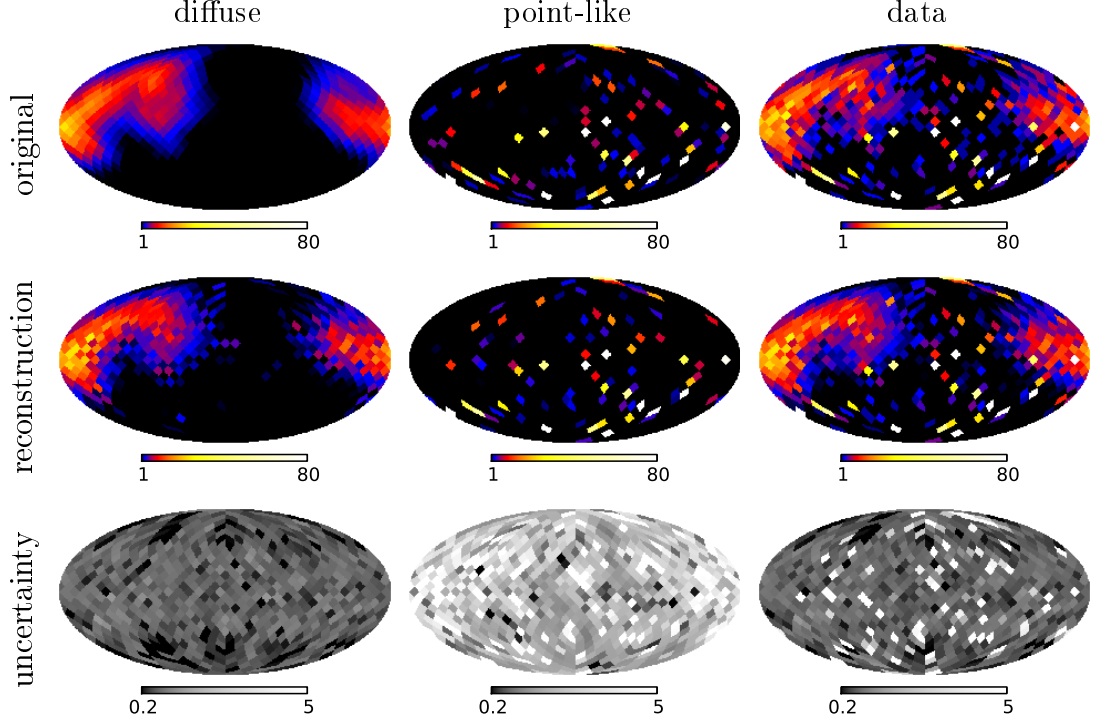
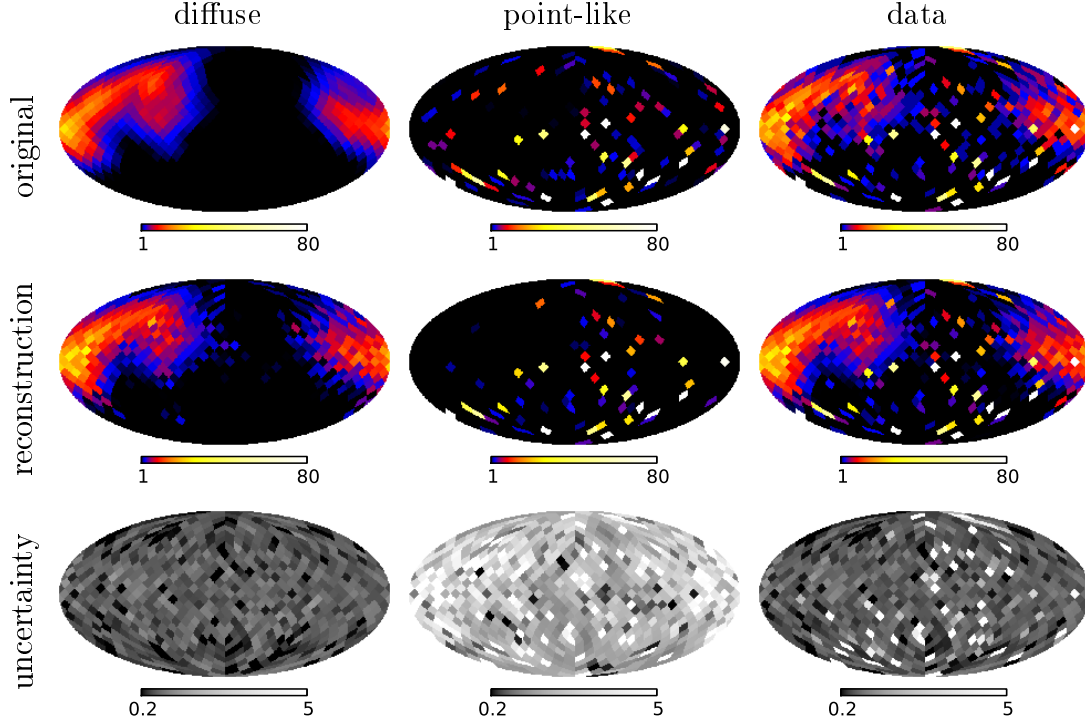


Figure 10: Reconstruction results at $T = 0.05$ presented in event maps with logarithmic scales: (1st row) the original diffuse and point-like signals, and the resulting data, (2nd row) the reconstructed maps for the diffuse and point-like emission, and the expected data from those, (3rd row) the pixelwise relative uncertainties for the reconstructions.²⁴

emission or which did not produce a single detected photon, are not reconstructed at all. On the other hand, the sensitivity of the point source reconstruction depends on the nearby diffuse flux causing a certain detection threshold. Again, the algorithm seems to perform slightly superior in the case of $T = 0.05$, where, despite a small number of falsely detected very faint sources, even in the regions with dominant diffuse flux almost all point-sources that appear reddish or brighter in Fig. 10 are correctly identified. The point-like uncertainties are correlated with the brightness of the diffuse emissivity, i.e. the relative standard deviations are higher in regions with higher diffuse flux. However, the inferred uncertainties are everywhere on a very high level, although the reconstruction agrees with the original. This is due to the numerical instability of the quantity \mathbf{r} that reads,

²⁴In order to clarify the labels consider e.g. the column with the diffuse source maps: the originally expected photon counts $\lambda_s = \mathbf{R} \exp(\mathbf{s})$, the according reconstruction $\langle \lambda_s \rangle_{(s,u|d)} \approx \mathbf{R} \exp(\mathbf{m}_s + \frac{1}{2} \hat{\mathbf{D}}_s)$ and relative standard deviation of the counts squared, i.e. $\langle \lambda_s * \lambda_s \rangle_{(s,u|d)}^c / \langle \lambda_s \rangle_{(s,u|d)}^2 \approx \exp(\hat{\mathbf{D}}_s) - 1$.

Figure 11: Same as Fig. 10, but for $T = 0.5$.

considering only one pixel, $r \propto (1 - d/\mu)$. So if the expected photon number μ comes close to the data d , this quantity easily changes sign during each step of the algorithm. Especially in pixels that host bright point-like sources, this change might be large causing numerical problems. The algorithm compensates by assigning a high variance \hat{D} and a rather low mean value m_u , whereas both contribute to the expectation value $\langle \lambda_u \rangle_{(s,u|d)} \approx \mathbf{R} \exp(m_u + \frac{1}{2} \hat{D}_u)$ and to $\mu = \langle \lambda_s + \lambda_u \rangle_{(\phi|D)}$. Those numerical flaws affect the correct presentation of the reconstruction errors. However, the use of subset optimization techniques focusing on bright sources and the incorporation of higher order corrections of the Gibbs free energy into the scheme may compensate for those problems.

In addition, remember that we chose an inverse-gamma distribution as a prior for the point sources in Sect. 4.2.4. in order to model their emissivity that follows a power-law. However, the Gaussian posterior ansatz models the photon flux as a log-normal distribution. This log-normal approximation exhibits an exponentially decreasing slope whereas the inverse-gamma distribution has a constant slope, here $\eta = 1.5$ for the point sources. If we ignore the influence of the likelihood for a moment, it is reasonable to expect high variances in the case one approximates the broad tail of our prior by the comparatively low one of a log-normal PDF. For

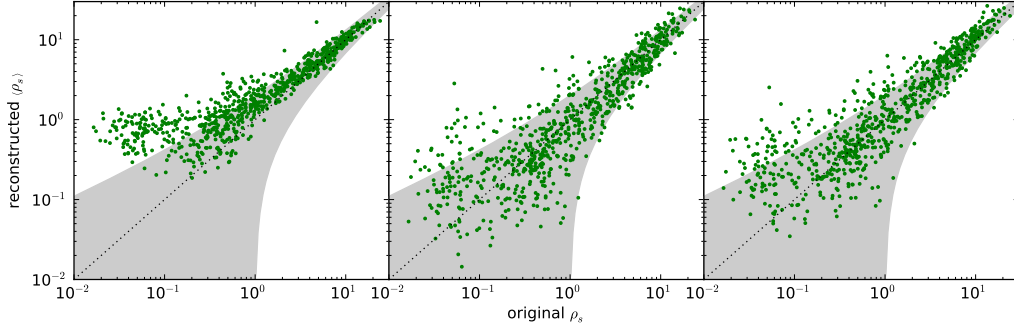


Figure 12: Comparison of the flux from diffuse sources: between (left) the pre-analysis, (middle) the reconstruction at $T = 0.05$, and (right) the reconstruction at $T = 0.5$. An ideal reconstruction would follow the (dotted) diagonal, the area of expected shot noise is highlighted (gray).

future approaches one could consider a deviation from the pure Gaussian posterior ansatz, e.g. a multi-temperature posterior [10].

The quantity $\boldsymbol{\mu}$, i.e. the expected data that would result from the reconstruction, agrees very well with the actual data \boldsymbol{d} indicating that the likelihood is satisfied. The high relative standard deviations of point sources shown in Fig. 10 and 11 single out those pixels in which the point-like contributions substantially stem from $\hat{\boldsymbol{D}}_{\boldsymbol{u}}$ for the aforementioned numerical reasons.

4.4.2. Comparison

It still remains to be clarified whether the obtained results are competitive to the outcomes of heuristic methods. Thus, the results obtained by the developed algorithm are compared with the ones from the pre-analysis. The pre-analysis relies on a standard technique, the identification of point sources by the difference between the data and their smoothed version exceeding a threshold. Scatter plots of the reconstructed versus the original flux are shown in Fig. 12 and 13 for the diffuse and point-like components, respectively.

Although the pre-analysis estimate for the diffuse signal is adequate, it is evidently biased towards higher flux estimates, especially in the less bright regions. This effect is due to the performed smoothing. However, the thermodynamically inferred signals are almost unbiased, only a vague trend can be seen in the reconstruction at $T = 0.5$. The wide spread of the inference results can again be explained by the numerical problems that cause those pixelated results.

The detection of point sources during the pre-analysis is limited due to the thresholding that becomes obvious in Fig. 13. The inference algorithm has no

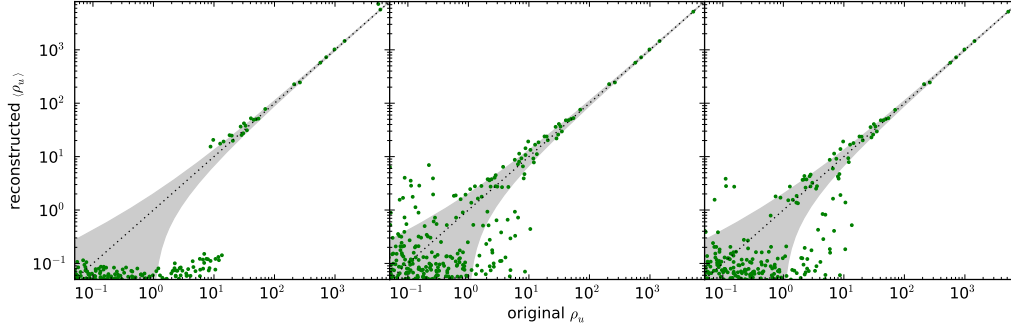


Figure 13: Same as Fig. 12, only for the flux from point sources.

such threshold and therefore reconstructs also fainter point sources. Further, we can see again that the results obtained at $T = 0.05$ slightly outperform the $T = 0.5$ case.

In summary it can be said, that the inference algorithm improves the outcomes of the pre-analysis and corrects their bias. Despite the numerical problems, the algorithm is considered to be competitive to such a standard technique.

4.5. Conclusions

The technique of thermodynamical inference with minimum Gibbs free energy is successfully applied to the problem of component separation. The developed algorithm performs excellently by providing separated reconstructions of the expected photon counts for both, diffuse and point-like, components. The diffuse result is mildly pixelated due to numerical flaws on small scales that could be resolved by subsequent smoothing or prevented by the implementation of an alternative, more robust library system like e.g. LIBPSHT [23] instead of HEALPIX. The results for the point-like sources suffer from numerical flaws, too. This inhibits a reliable error statement using $\hat{\mathbf{D}}_{\mathbf{u}}$, so far. However, the uncertainty estimates should be constrained by the incorporation of higher order corrections and the usage of subset optimization techniques focusing on the relevant pixels.

Furthermore, the algorithm performs well at both temperatures, although the $T = 0.05$ case slightly excels the $T = 0.5$ case. At the current state, the algorithm seems to prefer lower working temperatures. The implementation of higher order corrections may also allow the algorithm to operate at higher temperatures.

5. Conclusions & outlook

In this thesis the technique of thermodynamical inference is successfully applied within the framework of information field theory to the problem of morphological component separation in high energy astronomy. An algorithm is developed that reconstructs the photon flux from event maps and simultaneously separates the flux into the two fundamental classes of diffuse and point sources. In addition to this signal reconstruction, the algorithm provides an estimation of the corresponding uncertainties in terms of a covariance matrix.

The effective reconstruction and separation of the photon flux rely on the incorporation of all aspects relevant for the inference of the signals given the data. This involves on the one hand the superposition of the diffuse and point-like signal fields, the incorporation of the detector response and the implementation of local, i.e. pixelwise, shot noise due to the assumed Poisson statistics for photon counts. On the other hand, a description of the prior knowledge on the signal fields of interest is necessary. The diffuse signal is modeled by a multi-dimensional log-normal distribution with an a priori unknown spectrum that is also solved for during the reconstruction process. Furthermore, the point-like signal is described by pixel-independent inverse-gamma distributions with fixed shape and scale parameters.

Such a sophisticated inference involves a high level of computational complexity. One of the associated problems is the calculation of matrix diagonals. It is demonstrated that common stochastic estimates for matrix diagonals as appearing in inference problems can be improved by inference methods themselves.

A thermodynamical inference machinery for the main problem of reconstructing and separating the photon flux is detailed and applied to simulated data. The resulting reconstructed signal fields agree well with their originals. The diffuse reconstruction is accurate on large and intermediate scales. The reconstruction of the point sources enables the identification of bright and even faint sources. However, the precision of the current results is limited by an inflated uncertainty estimation and pixelated small-scale reconstructions of the diffuse component. Those effects are caused by numerical inaccuracies in the dependent code libraries and some of the simplifying assumptions made throughout the derivation of the algorithm. The implementation of an alternative, more robust library system, higher order corrections, and subset optimization techniques will hopefully overcome these limitations in the future.

Future expansions of the developed algorithm may include real instrumental responses, varying background rates due to cosmic ray events, and multiple energy bands in order to exploit additional spectral information on the sources. Moreover, the algorithm shall be applied to real data as e.g. provided by the ROSAT, INTEGRAL or Fermi survey.

A Notation

A1. Basic Notation

In this appendix a clarification of the basic notation introduced in Sect. 2. is given, first of all concerning the discretization of information fields. Due to technical reasons the data $\mathbf{d} = (d_i)_{i \in \{1, \dots, N_{\text{pix}}\}}$ will always be discrete, even if given in high-resolution, i.e. $N_{\text{pix}} \gg 1$. The scalar products defined in the data space are the usual Euclidean ones, i.e.

$$\mathbf{d}^\top \mathbf{d}' = \sum_{i=1}^{N_{\text{pix}}} d_i d'_i. \quad (106)$$

However, the signal field $\mathbf{s}(\tilde{x})$, that expresses information on physical quantities, might be defined over a continuous space $\Omega \ni \tilde{x}$, e.g. the surface of a unit sphere. A discretization of the space Ω into proper and pairwise disjoint subsets Ω_x indexed by $x \in \{1, \dots, r\}$ is convenient due to the implementation in a computational environment. This means for the field,

$$s_x = \mathcal{N}_x \int_{\tilde{x} \in \Omega_x} d\tilde{x} \, \varphi(\tilde{x}), \quad (107)$$

where x denotes the discretized coordinate and \mathcal{N}_x serves as a normalization constant. Further, the choice of \mathcal{N}_x is ambiguous and implies subtleties not to be underestimated. In order to emphasize this and the continuous interpretation of the signal field, the scalar product in the signal phase space is defined as follows,

$$\mathbf{s}^\top \mathbf{s}' = \int dx \, s_x s'_x, \quad (108)$$

where all normalization effects are incorporated into the integral measure dx . The intuitive choice of $\mathcal{N}_x = 1 / \int_{\tilde{x} \in \Omega_x} d\tilde{x}$ for pixelwise mean values is implemented in Sect. 3., whereas $\mathcal{N}_x = 1$ is chosen in Sect. 4. in order to integrate the considered photon flux and obtain photon counts.

Furthermore, throughout this thesis two different types of expectation values appear, the sample average $\langle \cdot \rangle_{\Xi}$ and the distribution weighted average $\langle \cdot \rangle_P$. The former denotes an arithmetic mean over a set $\Xi = \{\boldsymbol{\xi}\}$ of size $A = |\{\boldsymbol{\xi}\}|$, i.e.

$$\langle f(\boldsymbol{\xi}) \rangle_{\{\boldsymbol{\xi}\}} = \frac{1}{A} \sum_{a=1}^A f(\boldsymbol{\xi}^{(a)}), \quad (109)$$

where f is an arbitrary function. The latter denotes a path integral over the

complete phase space of the argument weighted by an appropriate probability distribution, e.g. for a prior $P(\boldsymbol{\varphi})$ weighted average, i.e.

$$\langle f(\boldsymbol{\varphi}) \rangle_{P(\boldsymbol{\varphi})} = \int \mathcal{D}\boldsymbol{\varphi} f(\boldsymbol{\varphi}) P(\boldsymbol{\varphi}). \quad (110)$$

Evidently, both averages are properly normalized so that $\langle 1 \rangle = 1$ holds.

A2. Special Notation

A2.1. Componentwise operations

The equations in Sect. 3. and 4. exhibit numerous componentwise operations. In order to keep the notation clear and simple it is convenient to write componentwise operations in an implicit way. Let $\boldsymbol{\varphi}$ and $\boldsymbol{\varphi}'$ be fields that were discretized with r pixels. The application of e.g. the exponential function to each component reads in such a convenient notation,

$$\exp(\boldsymbol{\varphi}) = (\exp(\varphi_1), \dots, \exp(\varphi_r))^\top. \quad (111)$$

The same notation is in effect for logarithms $\log(\boldsymbol{\varphi})$, quotients $\boldsymbol{\varphi}/\boldsymbol{\varphi}'$, etc. In order to avoid the risk of confusion between scalar products and the frequently appearing componentwise products, the latter is denoted with “ $*$ ”, i.e.

$$(\boldsymbol{\varphi} * \boldsymbol{\varphi}')_i = \varphi_i \varphi'_i \quad \forall i \in \{1, \dots, r\}. \quad (112)$$

Especially, it holds that $\boldsymbol{\varphi}^\top \boldsymbol{\varphi}' = \mathbf{1}^\top (\boldsymbol{\varphi} * \boldsymbol{\varphi}') \neq \boldsymbol{\varphi} * \boldsymbol{\varphi}'$.

A2.2. Diagonal operator

In Sect. 3. and 4. we make frequent use of matrix diagonals. Therefore, an abbreviatory notation for the diagonal of a matrix is introduced,

$$\hat{\mathbf{X}} = \text{diag}[\mathbf{X}] = (X_{11}, \dots, X_{rr})^\top, \quad (113)$$

where $\dim[\mathbf{X}] = r$. This notation implies the definition of a trivially linear operator that if applied to a matrix yields a vector and vice versa. However, this operation is not a projection since $\hat{\hat{\mathbf{X}}} \neq \hat{\mathbf{X}}$.

Nevertheless, the notation $\text{diag}[\cdot]$ is still reserved for longish expressions.

B Spherical Harmonics

The majority of problems addressed in this thesis are posed on the sphere and hence take a spherical symmetry as a basis. For this reason, the definition of spherical harmonics is clarified, and two relevant properties of a covariance matrix are shown assuming statistical isotropy.

B1. Basics

The orthonormal spherical harmonics are defined as

$$\mathcal{Y}_{lm}(\varphi, \theta) = \sqrt{\frac{2l+1}{4\pi} \frac{(l-m)!}{(l+m)!}} L_l^m(\cos \theta) e^{im\varphi}, \quad (114)$$

where $(\varphi, \theta) \equiv x$ are the spherical coordinates. The associated Legendre polynomials

$$L_l^m(\vartheta) = (-1)^m (1 - \vartheta^2)^{m/2} \frac{d^m}{d\vartheta^m} L_l(\vartheta), \quad (115)$$

are given by the unassociated Legendre polynomials

$$L_l(\vartheta) = \frac{1}{2^l l!} \frac{d^l}{d\vartheta^l} (\vartheta^2 - 1)^l. \quad (116)$$

The spherical harmonics fulfill the orthonormality relations,

$$\int d\Omega \mathcal{Y}_{lm}(\varphi, \theta) \mathcal{Y}_{l'm'}^*(\varphi, \theta) = \delta_{ll'} \delta_{mm'} \quad (117)$$

$$\sum_l \sum_{m=-l}^l \mathcal{Y}_{lm}(\varphi, \theta) \mathcal{Y}_{lm}^*(\varphi', \theta') = \delta(\varphi - \varphi') \delta(\cos \theta - \cos \theta'), \quad (118)$$

and more importantly the following addition theorem,

$$L_l(x^\top x') = \frac{4\pi}{2l+1} \sum_{m=-l}^l \mathcal{Y}_{lm}(x) \mathcal{Y}_{lm}^*(x'). \quad (119)$$

B2. Statistical isotropy

A probability distribution is statistically isotropic if and only if it is invariant under translation and rotation with respect to the reference system. A quantity drawn from a statistically isotropic distribution has therefore a position-independent ex-

pectation value, a covariance that only depends on the absolute distance between the two considered positions, etc. Further implications on the covariance matrix considering a spherical symmetry are discussed in the following subsections.

B2.1. Power spectrum

Consider a covariance matrix \mathbf{S} of a signal \mathbf{s} under some arbitrary but statistically isotropic PDF $P(\mathbf{s})$ in the spherical harmonics basis,

$$S_{(lm)(l'm')} = \langle s_{lm} s_{l'm'}^\top \rangle_{(\mathbf{s})} \quad (120)$$

$$= \int d\Omega d\Omega' \langle s(x) s(x') \rangle_{(\mathbf{s})} \mathcal{Y}_{lm}^*(x) \mathcal{Y}_{l'm'}(x'). \quad (121)$$

From the statistical isotropy of the signal \mathbf{s} follows that the covariance matrix only depends on the relative angle between the two positions, i.e. $\langle s(x) s(x') \rangle_{(\mathbf{s})} = S(x, x') = S(x^\top x')$. Ergo, each entry of the covariance matrix can be expanded in a series of Legendre polynomials,

$$\langle s(x) s(x') \rangle_{(\mathbf{s})} = \sum_{l''} \frac{2l'' + 1}{4\pi} C_{l''} L_{l''}(x^\top x'), \quad (122)$$

where $C_{l''}$ are the appropriate expansion coefficients. Applying the addition theorem given by Eq. (119),

$$S_{(lm)(l'm')} = \sum_{l''} \sum_{m=-l''}^{l''} C_{l''} \underbrace{\int d\Omega \mathcal{Y}_{l''m''}(x) \mathcal{Y}_{lm}^*(x)}_{\delta_{ll''} \delta_{mm''}} \underbrace{\int d\Omega' \mathcal{Y}_{l'm'}(x') \mathcal{Y}_{l''m''}^*(x')}_{\delta_{l'l''} \delta_{m'm''}} \quad (123)$$

$$= C_l \delta_{ll'} \delta_{mm'}, \quad (124)$$

the covariance matrix \mathbf{S} turns out to be diagonal in the spherical harmonics basis, i.e. an eigenbasis has been found. Those diagonal entries C_l are called the angular power spectrum of \mathbf{S} .

B2.2. Parameterization

The statistical isotropy of a covariance matrix \mathbf{S} implies not only a diagonal structure but furthermore a trivial block diagonal structure. Hence, it is convenient to

write \mathbf{S} as a direct sum,

$$\mathbf{S} = \bigoplus_l C_l \tilde{\mathbf{S}}_l = \begin{pmatrix} C_0 \tilde{\mathbf{S}}_0 & & 0 \\ & C_1 \tilde{\mathbf{S}}_1 & \\ 0 & & \ddots \end{pmatrix},$$

where the $(\tilde{\mathbf{S}}_l)_{mm'} = \delta_{mm'}$ are the identity matrices of the l -th spectral band in the spherical harmonics basis with a trace $\varrho_l = \text{tr}[\tilde{\mathbf{S}}_l^{-1} \tilde{\mathbf{S}}_l] = 2l + 1$ that equals the number of degrees of freedom for each spectral band.

The definition of $\mathbf{S}_l = \mathbb{0}_0 \oplus \cdots \oplus \mathbb{0}_{l-1} \oplus \tilde{\mathbf{S}}_l \oplus \mathbb{0}_{l+1} \oplus \cdots \oplus \mathbb{0}_{l_{\max}}$, where $\mathbb{0}$ stands for zero matrices, allows for extending the projections to the full dimension of \mathbf{S} which thus becomes a simple sum of the \mathbf{S}_l ,

$$\mathbf{S} = \sum_l C_l \mathbf{S}_l.$$

Analogously, the inverse matrices are defined, however \mathbf{S}_l^{-1} is then to be understood as a generalized or pseudoinverse of \mathbf{S}_l .

As a consequence the covariance matrix \mathbf{S} and its inverse can both be parameterized as follows,

$$\mathbf{S}^{\pm 1} = \sum_l C_l^{\pm 1} \mathbf{S}_l^{\pm 1} = \bigoplus_l C_l^{\pm 1} \tilde{\mathbf{S}}_l^{\pm 1}. \quad (125)$$

C Higher order corrections

The Gibbs free energy given by Eq. (96) in Sect. 4.3. inherits all corrections of order two and higher compressed into

$$\Delta^{(\nu_{\max})} = d^{\text{T}} \sum_{\nu=2}^{\nu_{\max}} \frac{(-1)^{\nu}}{\nu} [\text{I}]^{(\nu)} - \sum_l \gamma_l \sum_{\nu=2}^{\nu_{\max}} \frac{(-1)^{\nu}}{\nu} [\text{II}]_l^{(\nu)}. \quad (126)$$

The individual higher order terms of the Taylor expansion of the logarithms are

$$[\text{I}]^{(\nu)} = \left\langle \left(\frac{\mathbf{R}(\mathbf{e}^{\mathbf{m}_s + \boldsymbol{\varphi}} + \mathbf{e}^{\mathbf{m}_u + \boldsymbol{\psi}})}{\mathbf{R}(\mathbf{e}^{\mathbf{m}_s + \frac{1}{2} \hat{\mathbf{D}}_s} + \mathbf{e}^{\mathbf{m}_u + \frac{1}{2} \hat{\mathbf{D}}_u})} - \mathbf{1} \right)^{\nu} \right\rangle_{(\phi|\mathbf{D})} \quad (127)$$

$$[\text{II}]_k^{(\nu)} = \left\langle \left(\frac{q_l + \frac{1}{2} (\mathbf{m}_s + \boldsymbol{\varphi})^{\text{T}} \mathbf{S}_l^{-1} (\mathbf{m}_s + \boldsymbol{\varphi})}{q_l + \frac{1}{2} \text{tr}[(\mathbf{m}_s \mathbf{m}_s^{\text{T}} + \mathbf{D}_s) \mathbf{S}_l^{-1}]} - \mathbf{1} \right)^{\nu} \right\rangle_{(\phi|\mathbf{D})}. \quad (128)$$

After a lengthy, but not insightfully calculation one obtains the full second order correction to Eq. (96),

$$\begin{aligned}
 \Delta^{(2)} = & \sum_i \frac{d_i}{2} \left(\frac{1}{\left(\mathbf{R} \left(e^{\mathbf{m}_s + \frac{1}{2} \hat{\mathbf{D}}_s} + e^{\mathbf{m}_u + \frac{1}{2} \hat{\mathbf{D}}_u} \right) \right)_i^2} \right. \\
 & \times \left(\int dx dy R_{ix} R_{iy} e^{(\mathbf{m}_s)_x + (\mathbf{m}_s)_y + \frac{1}{2}((\mathbf{D}_s)_{xx} + 2(\mathbf{D}_s)_{xy} + (\mathbf{D}_s)_{yy})} \right. \\
 & + 2 \int dx dy R_{ix} R_{iy} e^{(\mathbf{m}_s)_x + (\mathbf{m}_u)_y + \frac{1}{2}((\mathbf{D}_s)_{xx} + 2(\mathbf{D}_{su})_{xy} + (\mathbf{D}_u)_{yy})} \\
 & \left. + \int dx dy R_{ix} R_{iy} e^{(\mathbf{m}_u)_x + (\mathbf{m}_u)_y + \frac{1}{2}((\mathbf{D}_u)_{xx} + 2(\mathbf{D}_u)_{xy} + (\mathbf{D}_u)_{yy})} \right) - 1_i \Bigg) \\
 & - \sum_l \frac{\gamma_l \text{tr} \left[(\mathbf{m}_s \mathbf{m}_s^\top + \frac{1}{2} \mathbf{D}_s) \mathbf{S}_l^{-1} \mathbf{D}_s \mathbf{S}_l^{-1} \right]}{2 \left(q_l + \frac{1}{2} \text{tr} \left[(\mathbf{m}_s \mathbf{m}_s^\top + \mathbf{D}_s) \mathbf{S}_l^{-1} \right] \right)^2}. \tag{129}
 \end{aligned}$$

This correction incorporates very strong correlations, as can be seen in terms like e.g. $(D_{xx} + D_{xy} + D_{yy})$ or $\text{tr}[\mathbf{D}_s \mathbf{S}_l^{-1} \mathbf{D}_s \mathbf{S}_l^{-1}]$. This enhanced entanglement increases the numerical effort for any solver, since one needs to calculate all entries of \mathbf{D} explicitly and not only its diagonal entries given by $\hat{\mathbf{D}}_s$ and $\hat{\mathbf{D}}_u$. Moreover one finds that the reidentification of the spectral parameters is strictly not possible any more since the corresponding terms now inherit an operator structure, cf. [10]. This makes it even harder to solve the numerical problem.

Nevertheless, all higher order corrections can be calculated in closed-form, although the complexity and the incorporated correlations increase rapidly with higher orders.

Acknowledgments

I thank Mike Bell, Fabrizia Guglielmetti, Henrik Junklewitz, Ewald Müller, Martin Reinecke, Georg Robbers, Maximilian Uhlig, Helin Weingartner and most notably Niels Oppermann for all the insightful discussions, productive comments and valuable advice on this thesis. Furthermore, Torsten Enßlin deserves my profound thanks for his outstanding supervision.

My special thanks go to my beloved family and Marie Uksa, who encouraged me throughout the thesis phase and cheered me up or calmed me down whenever necessary.

Further, I am indebted to the Technical University of Munich, especially the chair for experimental physics and astroparticle physics E15, as well as the Max Planck Institute for Astrophysics that enabled me to attend the conference “Statistical Challenges in Modern Astronomy V” and the preceding tutorial “Bayesian computation: MCMC and all that”.

Almost all of the computations related to this thesis have been executed by the free open-source mathematics software system SAGE²⁵. Some of the results in this work have been derived using the HEALPIX [12] package.

This research has made use of NASA’s Astrophysics Data System²⁶.

²⁵See SAGE homepage <http://www.sagemath.org/>

²⁶See ADS homepage <http://adswww.harvard.edu/>

References

- [1] E. Aune and D. P. Simpson. Parameter estimation in high dimensional Gaussian distributions. *ArXiv e-prints* stat.CO/1105.5256, May 2011.
- [2] C. Bekas, E. Kokiopoulou, and Y. Saad. An estimator for the diagonal of a matrix. *Applied Numerical Mathematics archive*, 57, November 2007.
- [3] E. Bertin and S. Arnouts. SExtractor: Software for source extraction. *A&A Spl.*, 117:393–404, June 1996.
- [4] G. Boole. *An Investigation of the Laws of Thought*. London: Walton and Maberly, 1854. Project Gutenberg eBook reprint (2005): <http://www.gutenberg.org/files/15114/15114-pdf.pdf>.
- [5] A. Caticha. Lectures on Probability, Entropy, and Statistical Physics. *ArXiv e-prints* physics.data-an/0808.0012, July 2008.
- [6] A. Caticha. Entropic Inference. In A. Mohammad-Djafari, J.-F. Bercher, & P. Bessière, editor, *American Institute of Physics Conference Series*, volume 1305 of *American Institute of Physics Conference Series*, pages 20–29, March 2011.
- [7] R. T. Cox. Probability, Frequency and Reasonable Expectation. *American Journal of Physics*, 14:1, January 1946.
- [8] T. A. Enßlin and M. Frommert. Reconstruction of signals with unknown spectra in information field theory with parameter uncertainty. *Phys. Rev. D*, 83(10):105014, May 2011.
- [9] T. A. Enßlin, M. Frommert, and F. S. Kitaura. Information field theory for cosmological perturbation reconstruction and nonlinear signal analysis. *Phys. Rev. D*, 80(10):105005, November 2009.
- [10] T. A. Enßlin and C. Weig. Inference with minimal Gibbs free energy in information field theory. *Phys. Rev. E*, 82(5):051112, November 2010.
- [11] E. B. Fomalont. A two-component log N-log S relationship. *Bull. Astr. Inst. Netherlands*, 20:69, August 1968.
- [12] K. M. Górski, E. Hivon, A. J. Banday, B. D. Wandelt, F. K. Hansen, M. Reinecke, and M. Bartelmann. HEALPix: A Framework for High-Resolution Discretization and Fast Analysis of Data Distributed on the Sphere. *ApJ*, 622:759–771, April 2005.

-
- [13] F. Guglielmetti, R. Fischer, and V. Dose. Background-source separation in astronomical images with Bayesian probability theory - I. The method. *MNRAS*, 396:165–190, June 2009.
 - [14] A. Haar. Zur Theorie der orthogonalen Funktionensysteme (Erste Mitteilung). *Mathematische Annalen*, 69:331–371, 1910.
 - [15] A. Haar. Zur Theorie der orthogonalen Funktionensysteme (Zweite Mitteilung). *Mathematische Annalen*, 71:38–53, 1911.
 - [16] J. A. Högbom. Aperture Synthesis with a Non-Regular Distribution of Interferometer Baselines. *A&A Spl.*, 15:417, June 1974.
 - [17] M. F. Hutchinson. A stochastic estimator of the trace of the influence matrix for laplacian smoothing splines. *Communications in Statistics - Simulation and Computation*, 18:1059–1076, 1989.
 - [18] E. T. Jaynes. Information Theory and Statistical Mechanics. *Physical Review*, 106:620–630, May 1957.
 - [19] E. T. Jaynes. Information Theory and Statistical Mechanics. II. *Physical Review*, 108:171–190, October 1957.
 - [20] S. Kullback and R. A. Leibler. On Information and Sufficiency. *The Annals of Mathematical Statistics*, 22(1):79–86, March 1951.
 - [21] N. Oppermann, H. Junklewitz, G. Robbers, and T. A. Enßlin. Probing magnetic helicity with synchrotron radiation and Faraday rotation. *A&A*, 530:A89, June 2011.
 - [22] N. Oppermann, G. Robbers, and T. A. Enßlin. Reconstructing signals from noisy data with unknown signal and noise covariance. *ArXiv e-prints astro-ph.IM/1107.2384*, July 2011.
 - [23] M. Reinecke. Libpsht - algorithms for efficient spherical harmonic transforms. *A&A*, 526:A108, February 2011.
 - [24] C. P. Robert, N. Chopin, and J. Rousseau. Harold Jeffreys’s Theory of Probability Revisited. *ArXiv e-prints math.ST/0804.3173*, April 2008.
 - [25] A. Rohde and A. B. Tsybakov. Estimation of high-dimensional low-rank matrices. *ArXiv e-prints math.ST/0912.5338*, December 2009.
 - [26] S. Rowan and J. Hough. Gravitational Wave Detection by Interferometry (Ground and Space). *Living Reviews in Relativity* - <http://www.livingreviews.org/lrr-2000-3>, 3:3, June 2000.

REFERENCES

- [27] M. Selig, N. Oppermann, and T. A. Enßlin. Improving stochastic estimates with inference methods: calculating matrix diagonals. *ArXiv e-prints astro-ph.IM/1108.0600*, August 2011.
- [28] J. R. Shewchuk. An Introduction to the Conjugate Gradient Method Without the Agonizing Pain. *Technical report, Carnegie Mellon University, Pittsburgh, PA*, 1994.
- [29] A. W. Strong. Maximum Entropy imaging with INTEGRAL/SPI data. *A&A*, 411:L127–L129, November 2003.
- [30] M. Su, T. R. Slatyer, and D. P. Finkbeiner. Giant Gamma-ray Bubbles from Fermi-LAT: Active Galactic Nucleus Activity or Bipolar Galactic Wind? *ApJ*, 724:1044–1082, December 2010.
- [31] J. M. Tang and Y. Saad. A probing method for computing the diagonal of a matrix inverse. *Numerical Linear Algebra with Applications*, April 2011.
- [32] A. R. Taylor, J. M. Stil, and C. Sunstrum. A Rotation Measure Image of the Sky. *ApJ*, 702:1230–1236, September 2009.
- [33] Y. Ueda, T. Takahashi, H. Inoue, T. Tsuru, M. Sakano, Y. Ishisaki, Y. Ogasaka, K. Makishima, T. Yamada, M. Akiyama, and K. Ohta. LOG N-LOG S Relations and Spectral Properties of Sources from the ASCA Large Sky Survey: Their Implications for the Origin of the Cosmic X-Ray Background (CXB). *ApJ*, 518:656–671, June 1999.
- [34] F. Valdes. Resolution classifier. In *Society of Photo-Optical Instrumentation Engineers (SPIE) Conference Series*, volume 331 of *Society of Photo-Optical Instrumentation Engineers (SPIE) Conference Series*, pages 465–472, October 1982.
- [35] C. Weig and T. A. Enßlin. Bayesian analysis of spatially distorted cosmic signals from Poissonian data. *MNRAS*, 409:1393–1411, December 2010.

Publication note

Parts of this work have been published in scientific journals or are in the process of publication:

1. M. Selig, N. Oppermann and T. A. Enßlin (2011): *Improving stochastic estimates with inference methods: calculating matrix diagonals*
2. M. Selig et. al. (in preparation): *Photon flux reconstruction and separation*²⁷

²⁷Subject to change without notice.

Statement of authorship

With the submission of this work I, Marco Selig, assure that I have autonomously authored the work and used none other but the specified resources.

Marco Selig

Garching, 2011-10-04